International Journal of Engineering Science 228 (2026) 104626

Contents lists available at ScienceDirect

International Journal of Engineering Science

journal homepage: www.elsevier.com/locate/ijengsci

Full length article

Wave-transformation interaction in polycrystalline martensitic transformation: A coupled phase-field-elastodynamic study

Xiaoying Liu [a,*], Daniel Schneider [a,b,c], Britta Nestler [a,b,c]

[a] Institute of Nanotechnology (INT-MSS), Karlsruhe Institute of Technology, Karlsruhe, 76131, Germany
[b] Institute for Applied Materials (IAM-MMS), Karlsruhe Institute of Technology, Karlsruhe, 76131, Germany
[c] Institute of Digital Materials Science (IDM), Karlsruhe University of Applied Sciences, 76133, Germany

ARTICLE INFO

Keywords:
Martensitic transformation
Polycrystalline material
Stress-induced transformation
Mechanical wave propagation
Phase-field-elastodynamic coupling
Variant selection

ABSTRACT

Martensitic transformation (MT) is a rapid displacive process characterized by lattice reconfiguration and transformation strain. While MT is commonly analyzed under quasi-static mechanical equilibrium assumptions, the abrupt lattice distortion inherent to the transformation acts as a dynamic mechanical source that emits transient stress waves. The role of these elastodynamic fields in regulating subsequent phase evolution in polycrystalline solids remains insufficiently understood. In this work, we develop a fully coupled phase-field-elastodynamic framework that integrates phase kinetics with explicit wave propagation resolved through a high-order orthogonal polynomial approximation. Within this formulation, transformation strains generate stress waves that propagate across grains and continuously reshape the local mechanical driving forces. The simulation results demonstrate that, compared with quasi-static conditions, inertia significantly alters the distribution of mechanical energy, thereby influencing nucleation behavior and variant growth dynamics. In polycrystalline systems, the phase-field-elastodynamic model reproduces key microstructural features, including spatially alternating variant arrangements, block partitioning within grains, and characteristic variant width and growth directions. The results obtained with inertia effects are in close agreement with theoretical predictions and experimental observations. These findings extend the conventional understanding of MT in polycrystalline materials.

1. Introduction

Martensitic transformation (MT) is a diffusionless, displacive phase transition central to the functional response of high-strength steels (Gong et al., 2025; Jiang et al., 2025; Wang et al., 2024; Yin et al., 2024) and shape memory alloys (Li et al., 2022, 2023; Zhang et al., 2023). In polycrystalline systems, martensitic nucleation preferentially occurs at stress concentrators, such as defects and grain boundaries (GB), and propagates via cooperative lattice shear, transforming austenite into martensite (Chen et al., 2024; Guo et al., 2024; P. Li et al., 2024). The associated transformation strain induces significant internal stresses and radiates transient mechanical waves, notably during the face-centered cubic (FCC) to body-centered cubic (BCC) transformation in steels (Chen et al., 2023; Lehnert et al., 2021) and the B2 to B19′ and FCC to hexagonal close-packed (HCP) transformations in shape memory alloys (Asmaa et al., 2025; Nataf et al., 2020; Weidner et al., 2021). Blaysat et al. (2020) reported that bursts of acoustic emission arise from the

* Corresponding author.
E-mail address: xiaoying.liu@kit.edu (X. Liu).

https://doi.org/10.1016/j.ijengsci.2026.104626
Received 19 May 2026; Received in revised form 25 June 2026; Accepted 28 June 2026
Available online 5 July 2026

transformation strain during MT, linked to the nucleation of phase domains and the advance of phase fronts. Lehnert et al. (2024) captured acoustic emission signals arising from the FCC to BCC MT using a broadband piezo sensor. Park et al. (2009) reported that the martensitic growth from FCC to BCC was completed within 100 ps for grains with a characteristic length scale of $\mathcal{O}(10\,\mathrm{nm})$, as observed using 4D electron microscopy. Using a nanosecond laser pulse and synchrotron diffraction, Schwabe et al. (2022) observed that the thermoelastic martensite-to-austenite transformation completed within 10 ns, and at least 80 % of austenite transformed to martensite within 200 ns, with heat-dissipation constraints likely masking an even faster intrinsic rate. These experimentally observed acoustic bursts indicate that mechanical waves are intrinsically coupled with transformation kinetics. However, how these transformation generated stress waves subsequently influence martensitic nucleation, growth and variant selection has remained unclear.

Conventional understanding of MT emphasizes quasi-static driving forces arising from thermal undercooling and applied stress (Arohi et al., 2024; J. Liu et al., 2021; Yang et al., 2024). Qian et al. (2024) reported a stress-induced MT with an ultralow critical stress, aimed at biomedical applications. Tyc et al. (2024) investigated how applied stress affects the MT and the resulting superelastic behavior. Zhou et al. (2023) examined an atypical stress-induced MT and its plasticity implications.

Recent studies have reported MTs induced by laser shocks (Gong et al., 2023; Lian et al., 2021; Xiao et al., 2025), ultrasonic impact (Ghasemi & Vanini, 2023; Sebdani et al., 2024; Su et al., 2024), plate impact (Hong et al., 2024; Jiao et al., 2023; Zhang et al., 2024), and terahertz-driven coherent lattice waves (Nagai et al., 2023; Zhou et al., 2021). However, these works primarily examine externally applied excitations. By contrast, stress waves generated almost instantaneously upon nucleation due to the abrupt lattice distortion, potent and transient mechanical pulses that propagate through the microstructure at the speed of sound, have received comparatively little attention. Although the roles of local stress states (Niessen et al., 2022; Zhang et al., 2025; Z. Zhang et al., 2023), crystallographic orientation (Liu & Wu, 2024; Sun et al., 2026; J. Wang et al., 2021), and GB constraints (Bauer et al., 2021; Li et al., 2024; Shimokawa et al., 2024) in polycrystals are well established, their coupled interaction with transformation-generated stress waves, and the resulting feedback on transformation kinetics, remain insufficiently understood. Such waves can interact with the surrounding austenite, perturb ongoing transformation fronts, and trigger new nucleation at microstructural interfaces (e.g., GB), pointing to a dynamic interaction between mechanics and transformation that complements conventional views of MT.

Because stress waves exhibit intrinsic spatiotemporal complexity and simulating phase evolution is computationally demanding, capturing the dynamic coupling between rapid wave propagation and phase evolution remains challenging. Phase-field modeling is robust and widely developed for MT (Dong et al., 2023; Ohmer et al., 2022; Xiong et al., 2022) and powerful for describing microstructural evolution and interfacial dynamics (Ansari et al., 2021; Lu et al., 2023; Montes de Oca Zapiain et al., 2021). Traditionally, however, it relies on quasi-static or inertia-free mechanical-equilibrium assumptions (Liu et al., 2023; Rezaee-Hajidehi et al., 2022; Tang & Miao, 2024; Zambrano et al., 2024; T. Zhang et al., 2023), which suppress elastodynamic effects. In recent years, phase-field frameworks have been advanced to probe the coupling between stress waves and phase transformations, and to model dynamic crack propagation (Kannenberg et al., 2024; Schneider et al., 2016; Schöller et al., 2022). Using a weak-form finite-element discretization with explicit time integration, Yao et al. (2024) examined how dynamic plasticity modulates phase-transition kinetics. With a first-order discontinuous Galerkin (DG) method to resolve elastic waves, Weinberg and Wieners (2022) investigated the initiation and evolution of dynamic fracture within a phase-field setting. Building on a space–time potential formulation and a time-discontinuous Galerkin scheme, Feutang et al. (2025) simulated the propagation of brittle cracks in an isotropic and elastic solid under dynamic loading. By coupling a phase-field perturbation model with Bloch–Floquet periodic boundary conditions, Zheng et al. (2025) elucidated the influence of 90° diffuse domain walls on Lamb-wave propagation in ferroelectric thin films.

In this work, we formulate a fully coupled phase-field-elastodynamic framework to resolve the dynamic interaction between transformation-strain-induced stress waves and stress-wave-driven MT in polycrystalline solids. By treating the transformation strain as a distributed mechanical source, the model captures both wave generation and wave-mediated modulation of phase kinetics in a unified manner. This approach enables the investigate of MT process in polycrystalline systems explicitly accounting for inertia effects. The simulation results show that elastodynamic effects do not merely accompany MT, but actively govern its spatiotemporal evolution in polycrystals. Compared with quasi-static simulations, inertia alters the distribution of mechanical energy, thereby influencing nucleation and variant distribution patterns. These findings extend conventional views of MT in polycrystals.

2. Methods

In this section, we provide a brief overview of the numerical methods, including the phase-field model for phase evolution (Section 2.1), the elastodynamic mechanical formulation (Section 2.2) and the quasi-static mechanical formulation (Section 2.3).

2.1. Phase-field model

In a multiphase system, the N-tuple $\boldsymbol{\phi} = \{\phi_\alpha, \phi_\beta, \dots, \phi_N\}$ is introduced as the set of order parameters, where ϕ_α represents the local volume fraction of phase α. Specifically, $\phi_\alpha = 1$ in the bulk regions of phase α and $\phi_\alpha = 0$ in the bulk regions of all other phases, whereas $0 < \phi_\alpha < 1$ in diffuse interface regions involving phase α. The Gibbs simplex constraint, $\sum_\alpha^N \phi_\alpha = 1$ with $0 \le \phi_\alpha \le 1$, is enforced through projection to ensure that the order parameters retain their physical meaning as local phase fractions (Daubner et al., 2023). Thus, the Ginzburg–Landau free energy functional $\mathcal{F}$ over the domain V can be expressed as the sum of the interfacial contribution $\mathcal{F}_{\mathrm{intf}}$ and the bulk contribution $\mathcal{F}_{\mathrm{bulk}}$ (Ginzburg & Landau, 2009):

$$\mathcal{F} = \underbrace{\int_V \left(\epsilon a(\nabla \boldsymbol{\phi}) + \frac{1}{\epsilon}\omega(\boldsymbol{\phi})\right) \mathrm{d}V}_{\mathcal{F}_{\mathrm{intf}}} + \underbrace{\int_V \left(f_{\mathrm{chem}}(\boldsymbol{\phi}) + f_{\mathrm{mech}}(\boldsymbol{\phi}, \boldsymbol{\varepsilon}, \boldsymbol{v})\right) \mathrm{d}V}_{\mathcal{F}_{\mathrm{bulk}}}, \tag{1}$$

where ϵ is the interface width parameter.

The gradient energy density is defined as Cahn and Hilliard (1958):

$$a(\nabla \boldsymbol{\phi}) = -\sum_{\alpha,\beta>\alpha} \gamma_{\alpha\beta} \nabla\phi_\alpha \cdot \nabla\phi_\beta, \tag{2}$$

with $\gamma_{\alpha\beta}$ denoting the interfacial energy between phases α and β.

The potential energy density is given by Cahn and Hilliard (1958):

$$\omega(\boldsymbol{\phi}) = \frac{16}{\pi^2} \sum_{\alpha,\beta>\alpha} \gamma_{\alpha\beta}\phi_\alpha\phi_\beta. \tag{3}$$

Let $f^{\alpha}_{\mathrm{chem}}$ denote the bulk chemical potential of phase α, which is constant at a fixed temperature, and let $h(\phi_\alpha) = \phi_\alpha$ be an interpolation function satisfying:

$$\sum_{\alpha} h(\phi_\alpha) = 1 \qquad 0 \le h(\phi_\alpha) \le 1. \tag{4}$$

The chemical energy density is then:

$$f_{\mathrm{chem}}(\boldsymbol{\phi}) = \sum_{\alpha} f^{\alpha}_{\mathrm{chem}} h(\phi_\alpha). \tag{5}$$

Assuming $\boldsymbol{\varepsilon}$ denotes the strain tensor in Voigt notation and $\boldsymbol{v}$ the material particle velocity vector, the mechanical energy density $f_{\mathrm{mech}}(\boldsymbol{\phi}, \boldsymbol{\varepsilon}, \boldsymbol{v})$ in Eq. (1) consists of two contributions, the elastic energy density $f_\varepsilon(\boldsymbol{\phi}, \boldsymbol{\varepsilon})$ and the kinetic energy density $f_v(\boldsymbol{\phi}, \boldsymbol{v})$:

$$f_{\mathrm{mech}}(\boldsymbol{\phi}, \boldsymbol{\varepsilon}, \boldsymbol{v}) = \underbrace{\sum_{\alpha} f^{\alpha}_{\varepsilon}(\boldsymbol{\varepsilon}^{\alpha}) h(\phi_\alpha)}_{f_\varepsilon(\boldsymbol{\phi},\boldsymbol{\varepsilon})} + \underbrace{\sum_{\alpha} f^{\alpha}_{v}(\boldsymbol{v}^{\alpha}) h(\phi_\alpha)}_{f_v(\boldsymbol{\phi},\boldsymbol{v})}. \tag{6}$$

Suppose $L_{\alpha\beta}$ denotes the mobility of the α-β interface. For each computational cell with $\tilde{N}$ active phases, the phase evolution of ϕ_α is governed by the following equation (Steinbach, 2009):

$$\frac{\partial \phi_\alpha}{\partial t} = -\frac{1}{\tilde{N}} \sum_{\substack{\beta=1 \\ \beta\neq\alpha}}^{\tilde{N}} L_{\alpha\beta} \left[\frac{\delta \mathcal{F}_{\mathrm{intf}}}{\delta \phi_\alpha} - \frac{\delta \mathcal{F}_{\mathrm{intf}}}{\delta \phi_\beta} + \frac{8\sqrt{\phi_\alpha\phi_\beta}}{\pi} \left(\frac{\delta \mathcal{F}_{\mathrm{bulk}}}{\delta \phi_\alpha} - \frac{\delta \mathcal{F}_{\mathrm{bulk}}}{\delta \phi_\beta} \right) + \epsilon \Delta \hat{a}_{\alpha\beta} \right] + \zeta_\alpha, \tag{7}$$

where

$$\frac{\delta \mathcal{F}_{intf}}{\delta \phi_\alpha} = \left(\frac{\partial}{\partial \phi_\alpha} - \nabla \cdot \frac{\partial}{\partial \nabla \phi_\alpha} \right) \left(\epsilon a(\boldsymbol{\nabla \phi}) + \frac{1}{\epsilon} \omega(\boldsymbol{\phi}) \right), \tag{8}$$

is the variational derivative of the interfacial free energy functional $\mathcal{F}_{intf}$.

For non-curvature-driven phenomena such as MT, the influence of curvature $\kappa = \nabla \cdot \left(\nabla\phi_\alpha / \left|\nabla\phi_\alpha\right| \right)$ should be minimized. To achieve this, an additional term $\epsilon \Delta \hat{a}_{\alpha\beta}$ is incorporated into the evolution equation, whereby the curvature contribution $\left|\nabla\phi_\alpha\right| \kappa$ is subtracted from the variational derivative of the gradient energy density (Schoof, 2021; Selzer, 2014):

$$\Delta \hat{a}_{\alpha\beta} = \gamma^{c}_{\alpha} \left(\nabla^2 \phi_\alpha - |\nabla \phi_\alpha| \kappa \right). \tag{9}$$

To ensure a consistent interplay between the gradient and potential energy densities, the interfacial energy in Eq. (3) is modified as follows:

$$\hat{\gamma}_{\alpha\beta} = \gamma_{\alpha\beta} + \gamma^{c}_{\alpha}. \tag{10}$$

A condition of $\gamma^{c}_{\alpha} \gg \gamma_{\alpha\beta}$ is required to establish a sufficient energy barrier between austenite and martensite, thereby stabilizing the diffuse interface under undercooling conditions (Chen et al., 2014; Schoof et al., 2018). It is worth noting that Eqs. (9) and (10) do not introduce any additional energetic contributions to the equilibrium state.

To enable the nucleation and growth of new martensitic variants, a seeding term ζ_α with amplitude A_ζ is introduced at the interfaces:

$$\zeta_\alpha = \begin{cases} \sum_{\beta,\eta>\beta} \phi_\beta \phi_\eta A_\zeta & (t \bmod t_\zeta = 0 \text{ and } \phi_\alpha = 0) \\ 0 & (\text{otherwise}), \end{cases} \tag{11}$$

where t_ζ is the time interval for the application of seeding. It is noted that the seeding term ζ_α is applied only when $\phi_\alpha = 0$, thereby enabling Eq. (7) to be activated for phase α in the subsequent time step. This is necessary because the evolution equation

is evaluated only for active phases at the interface. Unlike conventional Langevin-type thermal noise, which is commonly used to introduce stochastic fluctuations and is particularly suitable for studying thermally activated and statistically distributed nucleation events, Eq. (11) is employed as a deterministic seeding term. It introduces only a tiny fraction of new phases at diffuse interfaces in a controlled and reproducible manner, allowing the subsequent mechanically driven nucleation and evolution to be investigated and compared. To ensure that the nucleation and growth of martensitic variants are governed by the underlying energetics rather than numerical artifacts, the amplitude A_ζ must be sufficiently small, while the time interval t_ζ must be sufficiently large. Under this condition, the phase perturbations introduced by the seeding term ζ_α decay if the formation of the corresponding martensitic variants is not energetically favorable. A more detailed quantitative sensitivity analysis with respect to the amplitude A_ζ and time interval t_ζ is provided in Section 3.1.

By discretizing the computational domain into cubic cells on an equidistant grid, Eq. (7) is solved using a finite difference algorithm. The explicit Euler method is employed for time integration, in which the order parameters are updated using their spatially discretized values from the previous time step. To ensure numerical stability of this explicit scheme, the time step size Δt is chosen according to a Courant–Friedrichs–Lewy (CFL) type stability condition (Courant et al., 1928). Accordingly, Δt must be sufficiently small to resolve the interface evolution and to prevent changes in the order parameters from advancing over more than one computational cell within a single time step.

After the phase field is updated at each time step, the corresponding mechanical calculations are performed using the same uniform spatial grid and time step Δt. Therefore, the spatial and temporal discretizations introduced here are used consistently in the subsequent dynamic and static mechanical calculations and are not redefined in the following sections.

2.2. Elastodynamic mechanical formulation

This section presents the high-order DG method for stress-wave propagation (Section 2.2.1) and the formulation of transformation-strain-induced stress and velocity fields (Section 2.2.2) in the dynamic computations.

2.2.1. Governing equations for stress wave propagation

The governing equations for mechanical wave propagation, expressed in terms of the Voigt-vector representation of the stress tensor $\boldsymbol{\sigma}^{\mathrm{V}}$ and the velocity vector $\boldsymbol{v}$, are given as Dumbser and Käser (2006) and Käser and Dumbser (2006):

$$\dot{\boldsymbol{w}} = \boldsymbol{C}^1 \frac{\partial \boldsymbol{w}}{\partial x_1} + \boldsymbol{C}^2 \frac{\partial \boldsymbol{w}}{\partial x_2} + \boldsymbol{C}^3 \frac{\partial \boldsymbol{w}}{\partial x_3} + \boldsymbol{s}, \tag{12}$$

where $\dot{\boldsymbol{w}} = \partial \boldsymbol{w}/\partial t$ and $\boldsymbol{w} = \{\boldsymbol{\sigma}^{\mathrm{V}}, \boldsymbol{v}\}^{\mathrm{T}}$, the coefficient matrices $\boldsymbol{C}^i$ $(i = 1, 2, 3)$ are determined by the effective stiffness tensor and the effective density as given in Appendix, $\boldsymbol{x} = \{x_1, x_2, x_3\}^{\mathrm{T}}$ denotes the Cartesian coordinate system, and $\boldsymbol{s}$ represents the source term. It is worth noting that the stress–velocity form of mechanical wave governing equation, i.e., Eq. (12), is a first-order formulation equivalent to the conventional displacement-based wave equation together with the standard constitutive relation.

To ensure numerical accuracy in mechanical fields with complex temporal and spatial variations, each component of $\boldsymbol{w}$, i.e., w_i $(i = 1, 2, \ldots, 9)$, is approximated using orthogonal polynomials as:

$$w_i(\boldsymbol{x}, t) = \sum_{\substack{j,k,l \geq 0 \\ j+k+l \leq q}} c_i^{jkl}(t) p_j(x_1) p_k(x_2) p_l(x_3), \tag{13}$$

where $c_i^{jkl}(t)$ denotes the unknown coefficients at each time step, and $p_j(x)$ are orthogonal polynomials satisfying:

$$\int_{x_s}^{x_e} p_j(x) p_k(x) \mathrm{d}x = \begin{cases} 1 & (j = k) \\ 0 & (j \neq k), \end{cases} \tag{14}$$

within each computational cell bounded by $[x_s, x_e]$. Previous studies have demonstrated that high numerical accuracy and stability of the mechanical fields can be achieved with a polynomial order of $q = 3$ (Delcourte & Glinsky, 2015; X. Liu et al., 2021; Wilcox et al., 2010). Accordingly, the orthogonal polynomials $p(x)$ are constructed as:

$$\begin{cases} p_0(x) = 1 \\ p_1(x) = x - \frac{1}{2}(x_s + x_e) \\ p_2(x) = x^2 - (x_s + x_e)x + \frac{1}{6}(x_s^2 + x_e^2 + 4x_s x_e) \\ p_3(x) = x^3 - \frac{3}{2}(x_s + x_e)x^2 + \frac{3}{5}(x_s^2 + x_e^2 + 3x_s x_e)x - \frac{1}{20}(x_s + x_e)(x_s^2 + x_e^2 + 8x_s x_e). \end{cases} \tag{15}$$

With these high-order orthogonal polynomials, the weak form of Eq. (12) is explicitly solved at each time step for each cell over the entire computational domain, including both bulk and diffuse interface regions. As a result, the coefficient c_i^{ijk} for w_i is calculated

as Käser and Dumbser (2006) and X. Liu et al. (2021):

$$
\begin{aligned}
c_i^{jkl}(t+\Delta t) = c_i^{jkl}(t) + \\
\Delta t \Bigg(& \underbrace{\frac{1}{2}\int_S \sum_{m=1}^{3} \left((C_{in}^m - D_{in}^m) \left(\sum_{\substack{a,b,e\geq 0 \\ a+b+e\leq q}} c_n^{abe}(t) p_a(x_1) p_b(x_2) p_e(x_3) \right) p_j(x_1) p_k(x_2) p_l(x_3) \right) \mathrm{d}S}_{\text{Outgoing flux}} + \\
& \underbrace{\frac{1}{2}\int_S \sum_{m=1}^{3} \left((C_{in}^m + D_{in}^m) \left(\sum_{\substack{a,b,e\geq 0 \\ a+b+e\leq q}} c_n^{abe,S}(t) p_a(x_1) p_b(x_2) p_e(x_3) \right) p_j(x_1) p_k(x_2) p_l(x_3) \right) \mathrm{d}S}_{\text{Incoming flux}} - \\
& \underbrace{\int_V \sum_{m=1}^{3} \left(C_{in}^m \left(\sum_{\substack{a,b,e\geq 0 \\ a+b+e\leq q}} c_n^{abe}(t) p_a(x_1) p_b(x_2) p_e(x_3) \right) \frac{\partial p_j(x_1) p_k(x_2) p_l(x_3)}{\partial x_m} \right) \mathrm{d}V}_{\text{Volume integral}} + s_i^{jkl} \Bigg)
\end{aligned}
, \tag{16}
$$

where S and V denote the surface and volume of the current computational cell, respectively, and $c_n^{abe,S}(t)$ is the expansion coefficient of the neighboring cell sharing the surface S with the current cell. D_{in}^m is the element of the matrix $\boldsymbol{D}^m = \boldsymbol{G}^m \boldsymbol{H}^m (\boldsymbol{G}^m)^\top$, with $\boldsymbol{G}^m = (\boldsymbol{g}_1^m, \boldsymbol{g}_2^m, \dots, \boldsymbol{g}_9^m)$ and $\boldsymbol{H}^m = \mathrm{diag}(|h_1^m|, |h_2^m|, \dots, |h_9^m|)$. Here, the column vector $\boldsymbol{g}_i^m$ is the eigenvector corresponding to the eigenvalue h_i^m of the coefficient matrix $\boldsymbol{C}^m$, with the eigenvalues sorted as $h_i^m \leq h_j^m$ for $i < j$. The source term is given by $s_i^{jkl} = \dot{w}_i^{\mathrm{MT}}$ for $j = k = l = 0$, and $s_i^{jkl} = 0$ otherwise. The calculation of $\dot{w}_i^{\mathrm{MT}}$, which represents the MT-induced stress and velocity contributions, is introduced in Section 2.2.2.

In the present work, non-reflective boundary conditions are used for the elastodynamic simulations in Section 3. Under these conditions, the incoming flux in Eq. (16) is set to zero at the non-reflective boundary surfaces.

2.2.2. *Transformation-strain-induced stress and velocity*

In this phase-field-elastodynamic framework, the transformation strain is treated as the source of mechanical waves. Accordingly, the stress and velocity fields induced by MT are incorporated into Eq. (12) through the source term $\boldsymbol{s}$.

Because MT is completed on the timescale of $\mathcal{O}$(ps) to $\mathcal{O}$(ns), it is assumed that the change of total strain $\boldsymbol{\varepsilon}^V$ (in Voigt notation) due to MT is zero within each time step, i.e., $(\dot{\boldsymbol{\varepsilon}}^V)^{\mathrm{MT}} = (\dot{\bar{\boldsymbol{\varepsilon}}}^V)^{\mathrm{MT}} + \dot{\hat{\boldsymbol{\varepsilon}}}^V = \boldsymbol{0}$, where $\bar{\boldsymbol{\varepsilon}}^V$ and $\hat{\boldsymbol{\varepsilon}}^V$ respectively denote the elastic strain and the analogous transformation strain in Voigt notation. Therefore, the stress evolution $\dot{\boldsymbol{\sigma}}^V$ caused by MT is derived as:

$$
(\dot{\boldsymbol{\sigma}}^V)^{\mathrm{MT}} = -\boldsymbol{K}(\boldsymbol{\phi}) \dot{\hat{\boldsymbol{\varepsilon}}}^V(\boldsymbol{\phi}). \tag{17}
$$

Here, $\boldsymbol{K}(\boldsymbol{\phi})$ denotes the effective stiffness tensor, which coincides with the stiffness tensor of phase α in the bulk α regions. In diffuse interface regions, it is derived based on displacement continuity and mechanical equilibrium conditions at the corresponding sharp interface. Specifically, the tangential components of the strain tensor remain continuous across the sharp interface due to displacement compatibility, while the normal components of the stress tensor are continuous as required by force balance. Accordingly, the elastic energy is formulated in terms of these continuous stress and strain components, together with the phase-field variable $\boldsymbol{\phi}$, thereby avoiding nonphysical accumulation of elastic energy within the diffuse interface. On this basis, the effective stiffness tensor in diffuse interface regions can be directly obtained (Schneider et al., 2018, 2015). It is worth noting that $\boldsymbol{K}(\boldsymbol{\phi})$ evolves with the phase field and is updated from the current order parameter values at each time step. The temporal evolution of analogous transformation strain $\dot{\hat{\boldsymbol{\varepsilon}}}^V$ is expressed as:

$$
\dot{\hat{\boldsymbol{\varepsilon}}}^V(\boldsymbol{\phi}) = \begin{pmatrix} \sum_\alpha \tilde{\boldsymbol{\varepsilon}}_n^\alpha \dot{h}(\phi_\alpha) + \boldsymbol{C}_{nn}^{-1} \boldsymbol{C}_{nt} \sum_\alpha \tilde{\boldsymbol{\varepsilon}}_t^\alpha \dot{h}(\phi_\alpha) \\ (\boldsymbol{C}_{tt} - \boldsymbol{C}_{tn} \boldsymbol{C}_{nn}^{-1} \boldsymbol{C}_{nt}) \sum_\alpha \tilde{\boldsymbol{\varepsilon}}_t^\alpha \dot{h}(\phi_\alpha) \end{pmatrix}, \tag{18}
$$

where $\tilde{\boldsymbol{\varepsilon}}_n^\alpha$ and $\tilde{\boldsymbol{\varepsilon}}_t^\alpha$ denote, respectively, the normal and tangential components of the transformation strain of phase α. $\boldsymbol{C}_{nn}$, $\boldsymbol{C}_{nt}$, $\boldsymbol{C}_{tn}$ and $\boldsymbol{C}_{tt}$ are the four 3×3 submatrices of the stiffness tensor in its normal–tangential representation (Schneider et al., 2015).

In this phase-field-elastodynamic model, the transformation strain associated with MT induces not only stress fields but also velocity fields because inertia effects are explicitly considered. For the MT-induced velocity fields, it is essential to account for the propagation direction of the transformation front and that of the associated stress waves. Let $\boldsymbol{n} = (n_1, n_2, n_3)$ denote the outward unit normal of the austenite–martensite interface. The temporal evolution of the velocity field due to MT is calculated as Achenbach (2012):

$$
\dot{v}_i^{\mathrm{MT}} = V_P \dot{\bar{\varepsilon}}_{nn}^{\mathrm{MT}} n_i + 2V_S \left(\sum_{j=1}^{3} \dot{\bar{\varepsilon}}_{ij}^{\mathrm{MT}} n_j - \dot{\bar{\varepsilon}}_{nn}^{\mathrm{MT}} n_i \right), \tag{19}
$$

where the first term on the right-hand side represents the contribution of the longitudinal (P) wave, with V_P denoting the P-wave velocity, while the second term corresponds to the contribution of the shear (S) wave, with V_S denoting the S-wave velocity. $\dot{\hat{\varepsilon}}_{ij}^{\mathrm{MT}} = -\dot{\hat{\varepsilon}}_{ij}$, and $\dot{\hat{\varepsilon}}_{nn}^{\mathrm{MT}}$ represents the temporal evolution of the elastic strain normal to the austenite–martensite interface resulting from MT:

$$\dot{\hat{\varepsilon}}_{nn}^{\mathrm{MT}} = -\sum_{i=1}^{3}\sum_{j=1}^{3} n_i \dot{\hat{\varepsilon}}_{ij} n_j. \tag{20}$$

The contributions given by Eqs. (17) and (19) are incorporated into the right-hand side of Eq. (16) through the source term s_i^{jkl}.

2.3. Quasi-static mechanical formulation

For completeness, the quasi-static mechanical formulation is briefly introduced in this section. In the quasi-static case, the equilibrium condition:

$$\nabla \cdot \boldsymbol{\sigma} = \mathbf{0}, \tag{21}$$

the constitutive relation:

$$\boldsymbol{\sigma}^V = \boldsymbol{K}(\boldsymbol{\phi})(\boldsymbol{\varepsilon}^V - \hat{\boldsymbol{\varepsilon}}^V), \tag{22}$$

and the strain–displacement relation:

$$\boldsymbol{\varepsilon} = \frac{1}{2}\left(\nabla \boldsymbol{u} + (\nabla \boldsymbol{u})^{\mathrm{T}}\right), \tag{23}$$

are satisfied at each time step, where $\boldsymbol{u}$ denotes the displacement vector. After substituting Eqs. (22) and (23) into Eq. (21), the resulting equilibrium equation is solved implicitly using the finite element method. At each iteration, the residual vector $\boldsymbol{r}$ is evaluated as:

$$\boldsymbol{r} = \nabla \cdot \boldsymbol{\sigma}. \tag{24}$$

The iteration continues until the L_2-norm of the residual satisfies $\|\boldsymbol{r}\|_2 < 10^{-6}$, which is sufficiently small to ensure that quasi-static mechanical equilibrium is reached at each time step.

In the present work, roller supports are used as the boundary conditions for the quasi-static simulations. They are implemented by imposing $u_n = 0$ on the boundary surfaces, where u_n denotes the displacement component normal to the boundary.

3. Results

The MT process is investigated in this section. Section 3.1 presents a 1D benchmark study, comparing dynamic and quasi-static simulations for single- and two-grain systems. Section 3.2 examines a 2D domain consisting of two grains with different crystallographic orientations. Finally, Section 3.3 applies the proposed phase-field-elastodynamic model to polycrystalline systems and compares the results with those from quasi-static simulations.

3.1. 1D benchmark study

In Fig. 1, simulation results obtained from a two-grain domain are compared with those from a single-grain domain. In both cases, a 2 μm long computational domain is discretized into 200 uniform cells. For the two-grain configuration, the domain is divided into two austenite grains, denoted as A_1 and A_2. In contrast, the single-grain configuration consists entirely of a homogeneous austenitic phase, represented by A_1. In both configurations, a martensitic variant M_{11} is initialized at the left boundary within A_1 to investigate the influence of mechanical waves and GB upon the martensitic variant nucleation and growth. During the simulations, each austenite grain can transform into two martensitic variants, M_{i1} and M_{i2}, where i denotes the parent austenite grain. Non-reflective boundary conditions are applied at both the left and right boundaries.

The material properties for each phase and numerical parameters are summarized in Table 1. The density ρ and Young's modulus E are set as a representative for steels (Ball et al., 2024; Hilding & Schedin, 2002). During the FCC to BCC MT in steels, the process proceeds under rapid quenching in a diffusionless manner (Salama et al., 2025). The transformation occurs on the timescale of $\mathcal{O}$(ps) to $\mathcal{O}$(ns), which is much shorter than thermal equilibration (Park et al., 2009). Therefore, temperature evolution is neglected in the model. According to Eqs. (1) and (7), the chemical free energy provides the thermodynamic driving force for the phase transformation from austenite to martensite, while the mechanical energy governs the selection among competing martensitic variants. For a physically meaningful description of variant selection, the chemical and mechanical energy contributions should be of comparable magnitude, such that neither term overwhelmingly dominates the free-energy landscape. Based on the material parameters listed in Table 1, together with the typical strength and elastic properties of martensitic steels (Tian et al., 2025; Wang et al., 2021), the chemical driving force is set to $f_{\mathrm{chem}}^{\mathrm{M}} - f_{\mathrm{chem}}^{\mathrm{A}} = -6\times10^6\ \mathrm{J/m^3}$. This value is smaller than the thermodynamic estimates (10^7 to $10^8\ \mathrm{J/m^3}$) (Behjati & Najafizadeh, 2011; Moallemi et al., 2016). This reduction is motivated by the fact that the phase-field model resolves microstructural evolution at the micrometer scale and does not explicitly account for plastic relaxation, dislocation activity, lattice defects, or other dissipative mechanisms. As a consequence, the chemical driving force is treated as an effective

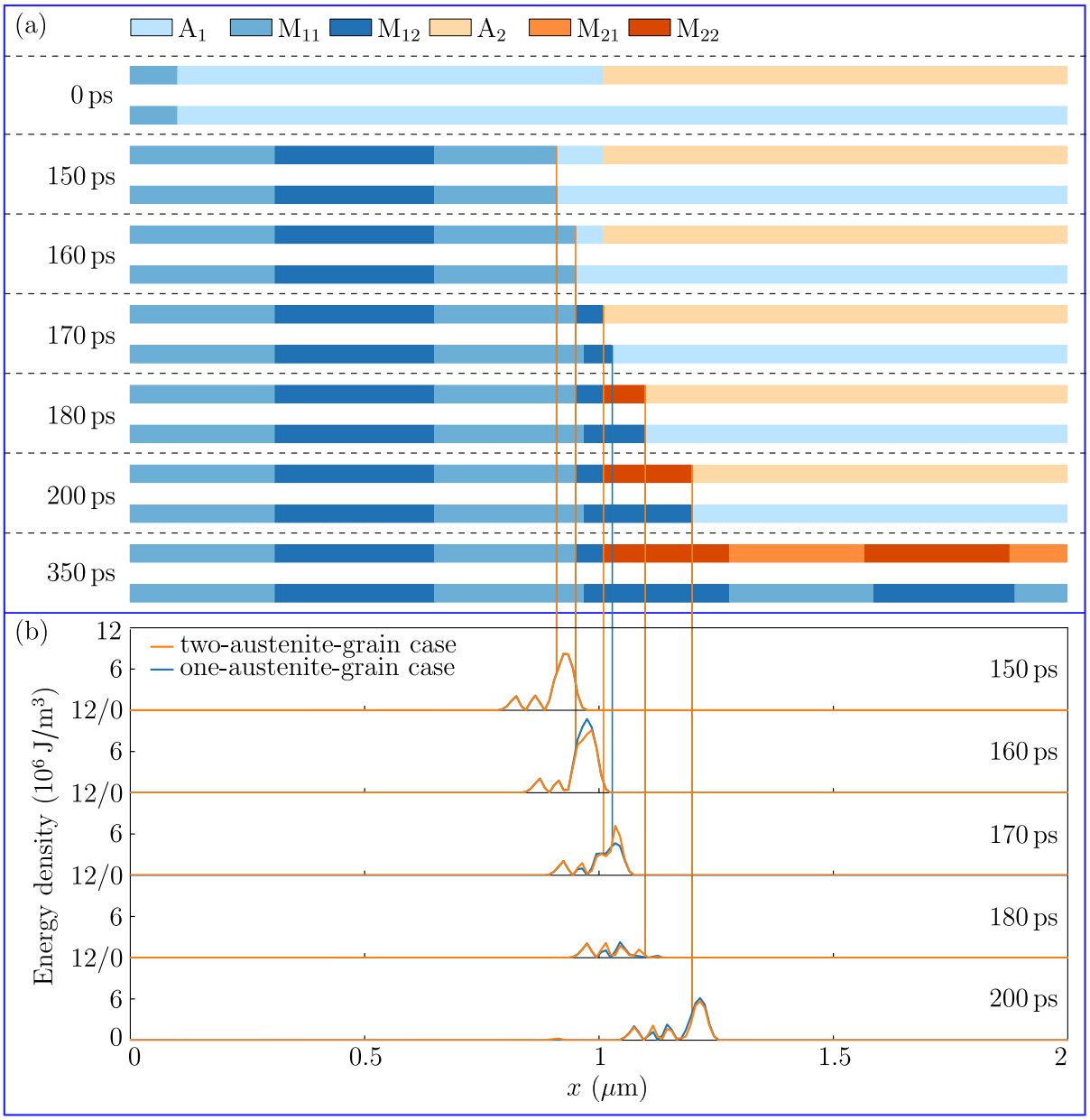

Fig. 1. MT in a 1D domain with and without a GB: (a) evolution of martensitic variants for the two-grain and single-grain cases at selected times; (b) comparison of energy density profiles between the two cases at corresponding times.

mesoscale parameter, representing only the portion of the thermodynamic driving force that contributes to interface motion and elastic interactions. The chosen value ensures that the elastic energy remains sufficiently influential to bias variant selection, while preserving the correct qualitative transformation behavior. Since this is a 1D simulation, the Poisson's ratio ν is set to zero, and only the transformation strains of the martensitic variants in the x-direction, i.e., $\tilde{\varepsilon}_{11}$, are non-zero. In the process of MT, part of the transformation strain is accommodated by plastic mechanisms, while only a fraction remains elastically stored. Accordingly, the transformation strain in the present model is interpreted as an effective eigenstrain. This reduced magnitude captures the elastic contribution of the transformation to stress wave generation and microstructural evolution (Chen & Shu, 2013). The mobility L_{AM} between austenite and martensite is set to ensure numerical stability and a well resolved diffuse interface, following established multiphase-field practice (Schoof et al., 2018; Steinbach, 2009). The transformation between martensitic variants is suppressed by setting $L_{\mathrm{M_1M_2}} = 0$. For MT in steels, interfacial energies in the range of $0.05\,\mathrm{J/m^2}$ to $0.4\,\mathrm{J/m^2}$ have been reported (Raabe et al., 2013; Salama et al., 2024; Zhang et al., 2020). In the present 1D model, an interfacial energy of $\hat{\gamma}_{\alpha\beta} = 0.09\,\mathrm{J/m^2}$ is adopted to ensure stable

Table 1
Simulation setup.

Phase	ρ (kg/m^3)	E (GPa)	$f^{\alpha}_{\mathrm{chem}}$ (J/m^3)	$\bar{\varepsilon}_{11}$	L_{AM} (10^{-3} m^4/(J s))	$\hat{\gamma}_{\alpha\beta}$ (J/m^2)	Δt (ps)	A_ζ	t_ζ (ps)
A	7800	200	0	0					
M_1	7800	200	-6×10^6	0.003	1.18	0.09	0.1	0.02	5
M_2	7800	200	-6×10^6	−0.003					

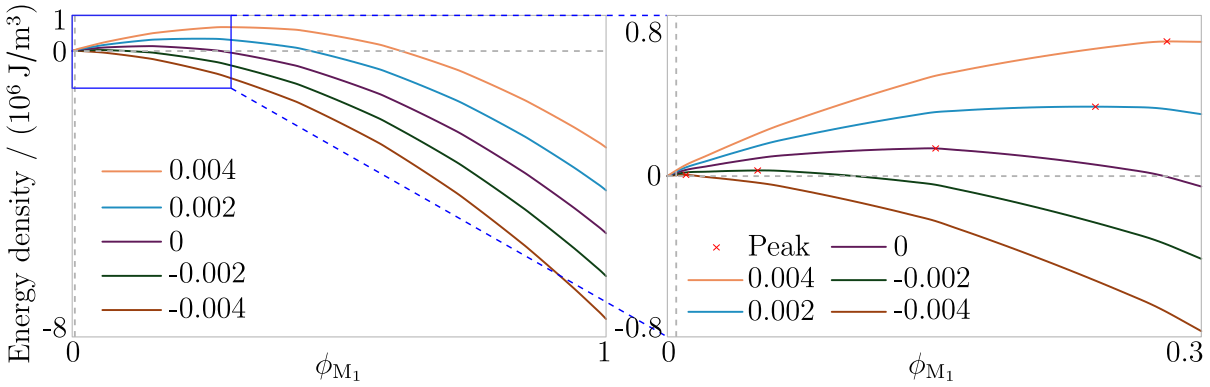

Fig. 2. Transformation pathways under different elastic strain conditions: (a) free energy density profiles along the transformation pathway from austenite to the representative martensitic variant M_1 under different strain states, referenced to the corresponding austenite energy, the horizontal dashed line indicates the austenite reference energy and the vertical dashed line at $\phi_{M_1} = 0.005$ denotes the maximum martensitic fraction introduced by the seeding term; (b) enlarged view of the early transformation stage ($0 \le \phi_{M_1} \le 0.3$).

numerical evolution of the diffuse interface. For numerical accuracy and stability in both the phase-field evolution and mechanical calculations, a time step size of $\Delta t = 0.1$ ps is used.

During the simulations, the seeding amplitude is fixed at 0.02, ensuring that the resulting local volume fraction of the newly introduced martensitic variant remains small, satisfying $\phi_{M_x} \le 0.005$. Under different elastic strain conditions, the transformation pathways from austenite to one representative martensitic variant M_1 are shown in Fig. 2(a), since the two martensitic variants are energetically symmetric. As the austenite free energy depends on the applied strain state, each transformation pathway is referenced to its corresponding austenite energy. Consequently, all energy profiles start from zero, enabling a direct comparison of the relative energy barriers and transformation pathways under different strain conditions. The horizontal dashed line represents the austenite reference energy, while the vertical dashed line at $\phi_{M_1} = 0.005$ denotes the maximum martensitic fraction introduced by the seeding term. For clearer visualization of the early transformation stage, Fig. 2(b) presents an enlarged view of the pathways in Fig. 2(a) for $0 \le \phi_{M_1} \le 0.3$. The peak value along each transformation pathway is marked by a red cross. It is observed that the martensitic fraction introduced by seeding is confined to the very early stage of the transformation. This seeding introduction enables the implementation of Eq. (7), according to which the martensitic fraction increases only if the transformation is energetically favorable and decreases otherwise. In the simulations, the seeding term is applied at the interfaces every 50 time steps, corresponding to a time interval of $t_\zeta = 5$ ps. Moreover, the small martensitic phase perturbation introduced by the seeding term vanishes within approximately 10 time steps if martensitic growth is not energetically favored. Therefore, the influence of seeding on the transformation energetics is negligible.

Fig. 1 at 150 ps shows that the microstructural evolutions in the two cases are identical until the transformation front reaches the interface between A_1 and A_2. The two martensitic variants nucleate and grow in an alternating manner. This behavior arises from the accumulation of mechanical energy during the growth of one variant, which eventually renders further growth energetically unfavorable. At this stage, the nucleation and initial growth of the other variant can release the accumulated mechanical energy, owing to their transformation strains having opposite signs. As the newly formed variant continues to grow, mechanical energy is re-accumulated, again suppressing its further growth and promoting the reactivation of the other variant. This cyclic process leads to the observed alternating growth behavior. At approximately 160 ps, the mechanical energy generated by the transformation strain of M_{11} reaches its maximum. This triggers the nucleation and growth of M_{12}, leading to the release of the accumulated mechanical energy, as shown in Fig. 1 at 170 ps. When the transformation front reaches the A_1–A_2 interface, M_{22} nucleates and grows in the first case, whereas the growth of M_{12} continues in the second case, as illustrated in Fig. 1(a) at 180 ps. In both cases, the growth of M_{12} or M_{22} leads to the release of mechanical energy, as shown in Fig. 1(b) at 180 ps. As growth proceeds, mechanical energy is re-accumulated as demonstrated in Fig. 1 at 200 ps. This cyclic process continues in each case until the entire domain transforms into martensite, as shown in Fig. 1(a) at 350 ps. The resulting martensitic morphologies in both cases are similar if the parent-phase index is neglected.

The simulation results under quasi-static mechanical conditions are presented in Fig. 3 for two cases: one with a single austenite grain A_1 and another with two grains A_1 and A_2, using the same configurations as in the dynamic mechanical case. However, the

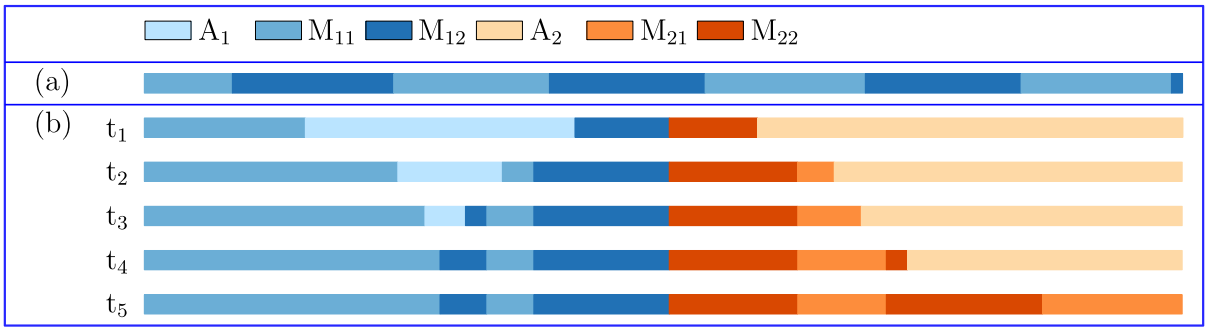

Fig. 3. MT in a 1D domain under quasi-static conditions: (a) single-grain domain; (b) two-grain domain.

boundary conditions in quasi-static case are set as roller supports in order to reach equilibrium. Since the mechanical energy is distributed throughout the entire domain in quasi-static case, the effective transformation strain must be increased to activate the MT. The first case, involving a single grain A_1, is used to generate martensitic variants with lengths comparable to those in the dynamic case (approximately 0.3 μm), as shown in Figs. 3(a) and 1(a). Accordingly, the transformation strain is set to 0.013 for variant M_1 and −0.013 for M_2. The interfacial energy is fixed at $0.05\,J/m^2$ to ensure a stable diffuse interface.

For the MT in the two-grain domain shown in Fig. 3(b), it should be noted that the labels t_1–t_5 indicate the transformation sequence rather than specific time values, as time is not explicitly considered under quasi-static mechanical conditions. In this case, the initial nucleation and growth of new variants occur at the A_1–A_2 interface, rather than at the transformation front as observed in the dynamic case, as illustrated in Fig. 3(b) at t_1. This behavior arises because the total volume fraction introduced by the seeding term, i.e., $\phi_{M_{12}} + \phi_{M_{22}}$, is higher at the A_1–A_2 interface than at the transformation front, where only $\phi_{M_{12}}$ is present. Consequently, a lower energy barrier needs to be overcome at the A_1–A_2 interface. Since the mechanical energy is nearly uniformly distributed throughout the domain, the A_1–A_2 interface becomes a more favorable site for nucleation. Subsequently, new martensitic variants nucleate and grow alternately in both grains until the entire domain transforms into martensite, as illustrated in Fig. 3 from t_2 to t_5. Under equilibrium conditions, the mechanical energy generated by local MT influences the nucleation and growth of variants throughout the entire domain. Consequently, the variant lengths vary depending on the MT processes occurring in both grains. As shown in Fig. 3(b) at t_5, the variant lengths in grain A_1 range from 0.08 to 0.58 μm, which deviates significantly from the well-defined lath structure typically observed in experiments (Krauss, 2017; Morito et al., 2006). After t_4, MT proceeds only in grain A_2, and the variants recover lengths of approximately 0.3 μm.

Therefore the proposed phase-field-elastodynamic model successfully reproduces the MT process in polycrystalline systems, capturing the spatially alternating distribution of martensitic variants and their evolution on a physically consistent time scale. Compared with quasi-static simulations, the dynamic formulation captures the concentration of mechanical energy associated with rapid displacive transformation, thereby ensuring well-structured variant distributions consistent with experimental observations.

3.2. 2D domain with two grains

Fig. 4 illustrates the MT process in a 2D domain of size 5 μm × 5 μm, discretized into 500 × 500 cells and initially composed of two equally sized austenite grains. The grain located in the lower-left region is labeled as A_1, while the one in the upper-right region is denoted as A_2. Grain A_2 is assigned three distinct crystallographic orientations, obtained by rotations of $\theta_i \in \{0°, 45°, 90°\}$ about the z-axis, hereafter referred to as Case I, Case II, and Case III, respectively. In each case, a M_{12} nucleus is predefined at the lower-left corner of the domain.

For this 2D domain, the material properties and numerical parameters that differ from those in Fig. 1 are summarized in Table 2. Since this is a 2D simulation, the Poisson's ratio ν is set to 0.3 as a representative for steels (Hilding & Schedin, 2002). In the full 3D crystallography of FCC to BCC MT with the Kurdjumov–Sachs orientation relationship, multiple martensitic variants exist. In the present 2D model, we adopt a reduced representation that retains the essential competition underlying variant selection by considering two variants with conjugate transformation strains. These strains correspond to a purely deviatoric shape change (zero trace), thereby emphasizing the shear dominated character of lattice reconfiguration in MT (Sreekala & Ananthakrishna, 2003). Similar to the 1D simulation in Section 3.1, the magnitude of transformation strains is set as an effective eigenstrain suitable for linear elastic coupling and for resolving variant competition without invoking additional inelastic accommodation mechanisms in a minimal model (Chen & Shu, 2013). The interfacial mobility L_{AM} is slightly adjusted to ensure the interfacial stability and a near sound speed evolution (Park et al., 2009; Steinbach, 2009). The interfacial energy $\hat{\gamma}_{\alpha\beta}$ is also adjusted within the suggested range to ensure the interfacial stability (Raabe et al., 2013; Salama et al., 2024; Zhang et al., 2020).

Fig. 4(a) illustrates the evolution of martensitic variants, whereas Fig. 4(b) shows the corresponding distributions of mechanical energy density and stress components. It is observed that the morphology of the martensitic variants and the distribution of mechanical energy density are identical in all three cases before the transformation front reaches the A_1–A_2 interface. Within grain A_1, the variant–variant interface appears as a line inclined at 45° to the horizontal direction. This orientation is consistent

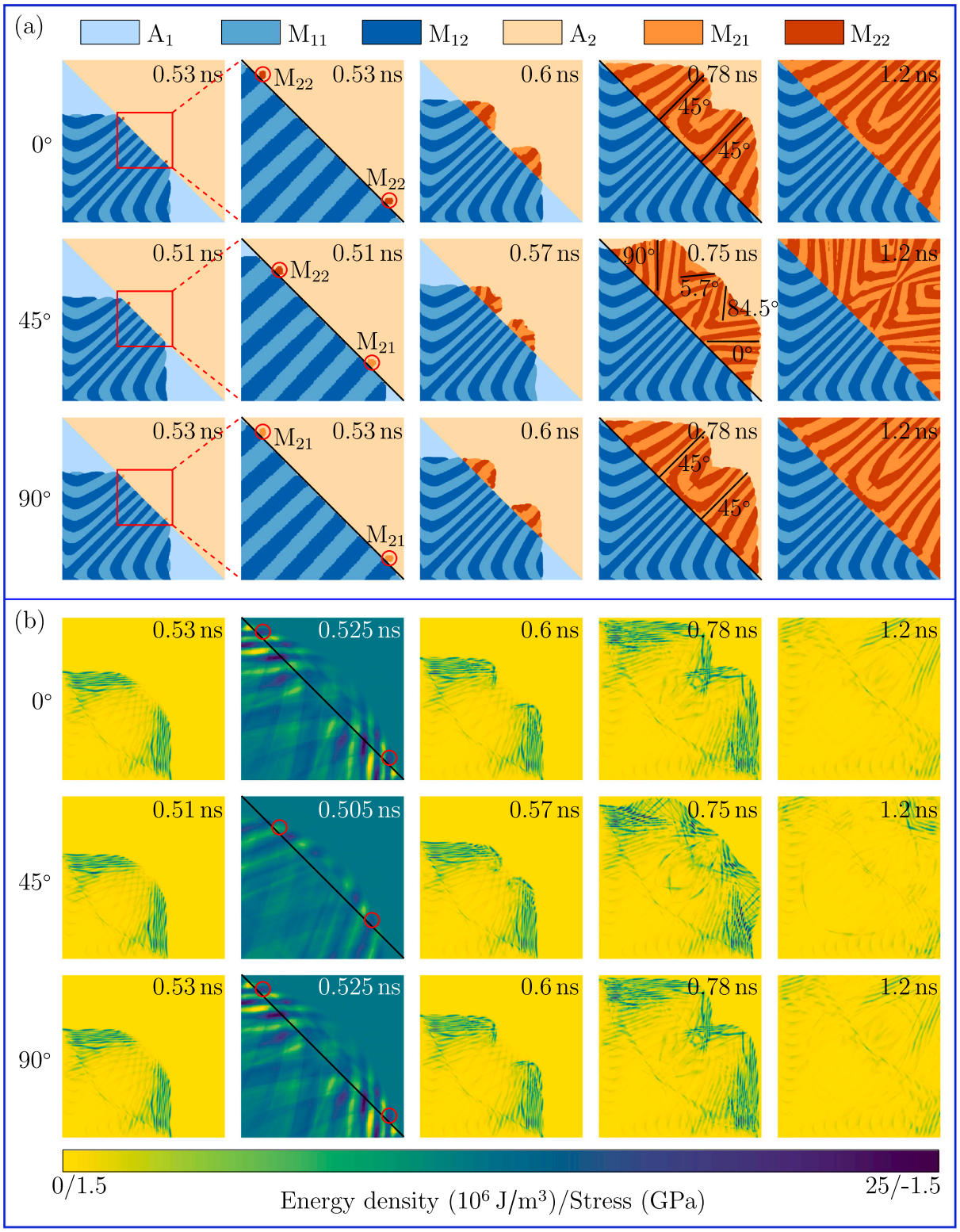

Fig. 4. Effect of grain orientation on MT: (a) time evolution of martensitic variants in a 2D domain containing two austenite grains, A_1 and A_2, where the orientation of A_2 is set to 0°, 45° and 90° in Cases I–III, respectively; (b) corresponding distributions of mechanical energy density (columns 1 and 3–5) and stress components prior to nucleation at the GB ($\sigma_{22} - \sigma_{11}$ for Cases I and III, and $2\sigma_{12}$ for Case II in column 2).

Table 2
Modified material properties and numerical parameters.

Phase	ν	$(\tilde{\varepsilon}_{11}, \tilde{\varepsilon}_{22}, \tilde{\varepsilon}_{12})$	L_{AM}	$\hat{\gamma}_{\alpha\beta}$
A	0.3	(0, 0, 0)	(10^{-3} m^4/(J s))	(J/m^2)
M_1	0.3	(−0.003, 0.003, 0)	1.48	0.11
M_2	0.3	(0.003, −0.003, 0)		

with theoretical prediction based on the kinematic compatibility condition for martensitic variants, as well as with experimental observations (Chapman et al., 2021; Shinohara et al., 2021, 2023). The directions of the variant–variant interfaces in other austenite grains with different rotation angles can be determined in the same manner.

The subfigures in the first column of Fig. 4(b) illustrate that the transformation-strain-induced mechanical wave propagates together with the transformation front, leading to a symmetric distribution of mechanical energy along the antidiagonal (from the lower left to the upper right corner) and a low mechanical energy density at the center of the domain. Consequently, no nucleation occurs when the martensitic variants located near the antidiagonal reach the A_1–A_2 interface, until approximately 0.53 ns or 0.51 ns, when the stress-wave peak arrives at the GB.

The central regions enclosed by the red squares in the first column of Fig. 4(a) are enlarged in the second column to illustrate the nucleation of new martensitic variants at the A_1–A_2 interface. The distribution maps of $\sigma_{22} - \sigma_{11}$ in Cases I and III and $2\sigma_{12}$ in Case II at the time when nucleation begins are shown correspondingly in the second column of Fig. 4(b), where the locations of the M_{21} and M_{22} nuclei are marked by red circles. Based on the transformation strains listed in Table 2, it can be derived that the driving force contributed by mechanical energy for M_{21} is:

$$\Delta\mathcal{G}^{\mathrm{mech}}_{\mathrm{M}_{21}} = (\sigma_{22} - \sigma_{11}) \cdot 0.03 \cos 2\theta - 2\sigma_{12} \cdot 0.03 \sin 2\theta, \tag{25}$$

while $\Delta\mathcal{G}^{\mathrm{mech}}_{\mathrm{M}_{22}} = -\Delta\mathcal{G}^{\mathrm{mech}}_{\mathrm{M}_{21}}$. Therefore, in Case I, variant M_{21} is energetically preferred if $\sigma_{22} > \sigma_{11}$, whereas variant M_{22} is favored if $\sigma_{22} < \sigma_{11}$, since both variants share identical interfacial energies and chemical driving force. In Case III, this energetic preference is reversed, with M_{22} favored for $\sigma_{22} > \sigma_{11}$ and M_{21} preferred for $\sigma_{22} < \sigma_{11}$. In Case II, the variant selection is governed by the shear stress $2\sigma_{12}$: M_{22} is energetically favored for $2\sigma_{12} > 0$, while M_{21} becomes preferred for $2\sigma_{12} < 0$. Consequently, as shown in the second column of Fig. 4, when $\sigma_{22} - \sigma_{11}$ reaches about −510 MPa at $t = 0.525$ ns at the A_1–A_2 interface, two M_{22} nuclei grow in Case I, whereas two M_{21} nuclei appear in Case III. In Case II, $2\sigma_{12}$ reaches 577 MPa within the upper circle and −577 MPa within the lower circle at $t = 0.505$ ns. As a result, one M_{22} nucleus emerges within the upper circle, while one M_{21} nucleus grows within the lower circle. It is also observed that two M_{21} nuclei grow at the phase fronts of M_{11} in Case I, as they share the same transformation strains. In contrast, two M_{22} nuclei appear at the same positions in Case III, because the transformation strains of M_{21} and M_{22} are interchanged as the orientation of grain A_2 is set to 90°.

As the MT proceeds in grain A_2, new martensitic nuclei form along the A_1–A_2 interface toward both corners, driven by the arrival of stress-wave peaks at the interface, as shown in the third column of Fig. 4. Meanwhile, the initially formed M_{21} and M_{22} nuclei grow not only into grain A_2, but also toward the center of the domain, driven by the chemical potential. Accordingly, the martensitic variants in Cases I and III exhibit growth directions of approximately ±45° relative to the horizontal (fourth column of Fig. 4(a)), consistent with theoretical predictions based on the kinematic compatibility condition. In Case II, the variants are expected to form M_{21}–M_{22} interfaces oriented at 0° and 90° relative to the horizontal direction. However, due to constraints imposed by the GB and the complex distribution of mechanical energy density, the growth directions of M_{21} and M_{22} deviate slightly, by approximately 5°, from the theoretical prediction.

The mechanical wave front propagates in tandem with the transformation front, as shown in the fourth column of Fig. 4(b). The corresponding distribution maps of mechanical energy density become increasingly complex owing to the concurrent growth of martensitic nuclei and the overlap of stress waves. This interaction renders the MT behavior more intricate if additional austenitic interfaces are present, such as in the polycrystalline domain described in Section 3.3.

At $t = 1.2$ ns, the entire domain has transformed from austenite to martensite, with the martensitic variants arranged alternately in space and clearly influenced by grain orientation, as demonstrated in the last column of Fig. 4(a). The mechanical wave continues to propagate outward from the domain boundaries due to the use of non-reflective boundary conditions, as shown in the last column of Fig. 4(b).

In summary, martensitic nucleation at GB occurs only if the local mechanical energy density is sufficiently high to overcome the energy barrier between the austenite and martensite phases. Variant selection is governed by the combined effects of stress components, transformation strain and grain orientation. Considering these factors, the variant that minimizes the mechanical energy can be identified, thereby completing the selection process. The simulation results are consistent with the theoretical derivation. Furthermore, the growth directions of martensitic variants obtained from simulations agree well with theoretical predictions based on the kinematic compatibility condition, as well as with available experimental observations.

3.3. Martensitic transformation in polycrystalline systems

Fig. 5 illustrates the MT process in a polycrystalline domain with dimensions of 20 μm × 20 μm, which is discretized into 2000 × 2000 cells and initially consists of 12 austenite grains. The grains are grouped into four crystallographic orientation classes,

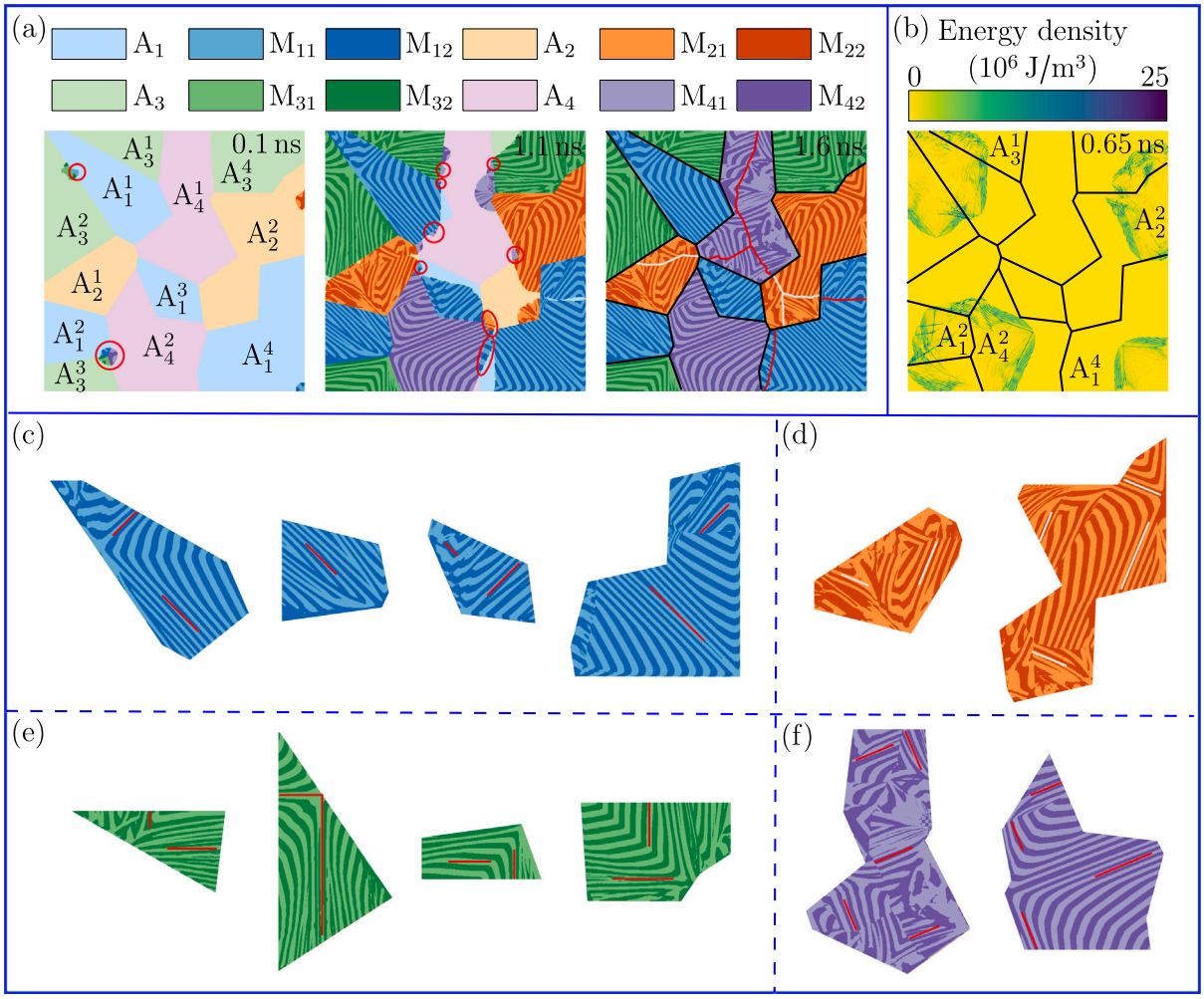

Fig. 5. MT in a polycrystalline domain with multiple nuclei and irregular GB: (a) evolution of martensitic variants at $t = 0.1$ ns, 1.1 ns and 1.6 ns in a 12-grain system with four orientation classes ($\theta_i \in 0°$, 22.5°, 45° and 67.5°); (b) mechanical energy density distribution at $t = 0.65$ ns; (c–f) martensitic morphologies within austenite classes A_1–A_4, respectively.

i.e., $\theta_i \in \{0°, 22.5°, 45°, 67.5°\}$. Each austenite grain is denoted as A_i^j, where i indexes the orientation θ_i and j enumerates the grains sharing that orientation. The martensitic variants within grain A_i^j are accordingly labeled as M_{i1}^j and M_{i2}^j. Four martensitic nuclei are predefined at representative point sites: in grain A_3^2 at a two-grain interface, in A_4^2 at a triple junction, in A_2^2 at the domain boundary, and in grain A_1^4 at a corner. Hereafter, these four sites are denoted by N_1, N_2, N_3, and N_4, respectively. The numerical parameters and material properties are identical to those used in Section 3.2.

At $t = 0.1$ ns in Fig. 5(a), new martensitic nuclei appear and begin to grow at N_1 and N_2, almost immediately following the expansion of the predefined nuclei. This occurs because the transformation-strain-induced mechanical waves propagate rapidly into the neighboring austenite grains once the predefined nuclei at N_1 and N_2 start to grow. At $t = 1.1$ ns, as shown in Fig. 5(a), additional nuclei emerge at several sites along the GB (highlighted with red circles), driven by these propagating waves. This process significantly increases the complexity of the mechanical energy density distribution and leads to a correspondingly intricate martensitic morphology. By $t = 1.6$ ns, the entire domain has transformed from austenite to martensite. The major impingement lines, where transformation fronts meet, are marked in red and gray. These impingement lines partition the original austenite grains into distinct blocks, each containing martensitic variants with different spatial distribution patterns.

The martensitic morphologies within each austenite grain are shown in Fig. 5(c–f) for austenite classes A_1–A_4, respectively. Based on the transformation strain characteristics listed in Table 2 and the crystallographic orientations of the austenite classes, two theoretical martensitic growth directions are derived for each class according to the kinematic compatibility condition, as summarized in Table 3. These predicted growth directions are indicated by red and gray lines within each grain. The simulation results show that martensitic variants generally grow along these directions. Notably, these theoretical predictions do not account for additional factors that complicate the mechanical energy distribution, such as concurrent nucleation and growth at GB and

Table 3
Martensitic growth directions.

	A_1	A_2	A_3	A_4
Martensitic growth direction	−45° 45°	−22.5° 67.5°	0° 90°	22.5° −67.5°

the impingement of transformation fronts within grains. Under the combined influence of these factors, the martensitic variants are subdivided into several blocks in most grains, and the actual growth directions exhibit slight deviations from the theoretical predictions, consistent with experimental observations (Nambu et al., 2013; Shinohara et al., 2021; Zhang et al., 2017).

To gain insight into the relationship between the transformation-strain-induced mechanical waves and the growth of martensitic variants, Fig. 5(b) presents the mechanical energy density at $t = 0.65$ ns. The energy density exhibits a chaotic distribution in some regions due to the presence of multiple nuclei, such as in grain A_3^1, at the bottom of grain A_1^2 and at the top-left of grain A_2^2. Consequently, the martensitic variants in these regions grow in directions that deviate from the theoretical ones, as shown in Fig. 5(c–f). In contrast, regular distributions of mechanical energy are observed in grains such as A_4^2, A_1^4, and at the top-right of grain A_2^2. As a result, the martensitic variants in these regions grow approximately along the theoretical directions. The multiple nuclei and impingement lines observed at $t = 1.1$ ns and 1.6 ns in Fig. 5(a) indicate a complex interaction between the mechanical waves and the MT in grain A_4^1. Consequently, the martensitic variants in this grain are discretized into multiple blocks, as shown in Fig. 5(f).

The simulation results under quasi-static mechanical conditions are presented in Fig. 6. To obtain comparable variant widths, the effective transformation strains are set to (−0.01, 0.01, 0) for variant M_1 and (0.01, −0.01, 0) for M_2. The interfacial energy is fixed at $0.07\,J/m^2$ to ensure a stable diffuse interface. Roller boundary conditions are applied. All other numerical parameters are identical to those used in the dynamic case. Consistent with the 1D quasi-static case, nucleation initiates at GB prior to the arrival of the transformation fronts, as shown in Fig. 6(a) at t_1. Nucleation preferentially occurs at triple junctions, where the total volume fraction introduced by the seeding term is higher, resulting in a lower energy barrier for nucleation, analogous to the 1D case. As the transformation proceeds, variant widths become irregular because nucleation and growth events throughout the domain influence the local transformation behavior, as illustrated in Fig. 6(a) at t_2 and t_3. Consequently, blocks with uniform variant width are unlikely to form under quasi-static mechanical conditions, particularly once multiple nucleation and growth sites are active. By t_3, the domain is fully transformed into martensite, with the majority of variant widths spanning a broad range of 0.08 to 0.83 μm. Fig. 6(b–e) demonstrate that the variant growth directions closely follow the theoretical predictions, exhibiting negligible deviation.

In summary, the proposed phase-field-elastodynamic model successfully reproduces the MT process in polycrystalline systems, explicitly accounting for inertia effects associated with rapid displacive transformations. The austenite grains are partitioned into distinct blocks characterized by different variant distribution patterns. The martensitic variants exhibit a spatially alternating arrangement and grow approximately along the theoretically predicted directions. Compared with quasi-static simulations, the dynamic formulation yields blocks with more uniform variant widths (around 0.3 μm), owing to the localized distribution of mechanical energy, in closer agreement with experimental observations.

4. Conclusion

In this work, a fully coupled phase-field–elastodynamic framework is employed to investigate MT in polycrystalline systems, explicitly accounting for inertia effects associated with rapid displacive transformations. In this formulation, transformation strains are treated as distributed dynamic sources, enabling simultaneous resolution of phase kinetics and stress wave propagation.

The results demonstrate that elastodynamic effects fundamentally alter the distribution of mechanical energy, thereby influencing the MT process. In contrast to quasi-static simulations, where mechanical energy is uniformly distributed throughout the domain and transformation events are globally coupled, the dynamic formulation produces localized energy concentrations that govern martensitic nucleation, variant selection and growth. Nucleation events at GB are triggered if stress waves reach the GB with sufficient mechanical energy. As a result, the initial austenite grains are partitioned into distinct blocks. Within each block, the martensitic variants exhibit a spatially alternating arrangement with characteristic widths of approximately 0.3 μm, whereas under quasi-static conditions the majority of variant widths span a broad range of 0.08 to 0.83 μm. The variant growth directions agree well with theoretical predictions based on kinematic compatibility, with slight deviations arising from complex interactions between stress waves and GB. Generally, the microstructural features reproduced by the coupled phase-field–elastodynamic framework are in good agreement with experimental observations. It should be noted, however, that quasi-static phase-field models remain appropriate when mechanical relaxation occurs on a much shorter timescale than phase evolution, such that the phase field responds primarily to the relaxed mechanical equilibrium state rather than to transient inertial fields. This may occur, for example, when elastic waves rapidly leave the relevant region or are sufficiently attenuated before they significantly affect nucleation, variant selection or interface motion.

Several limitations of the current model should be acknowledged. First, plastic deformation is not explicitly considered. In real materials, inelastic relaxation may attenuate stress waves and modify local driving forces. Second, the present simulations employ effective transformation strains and reduced crystallographic representations, which capture the essential features of variant competition but neglect the full multiplicity of variants in 3D systems. Incorporating plasticity and full crystallography therefore represents an important direction for future work.

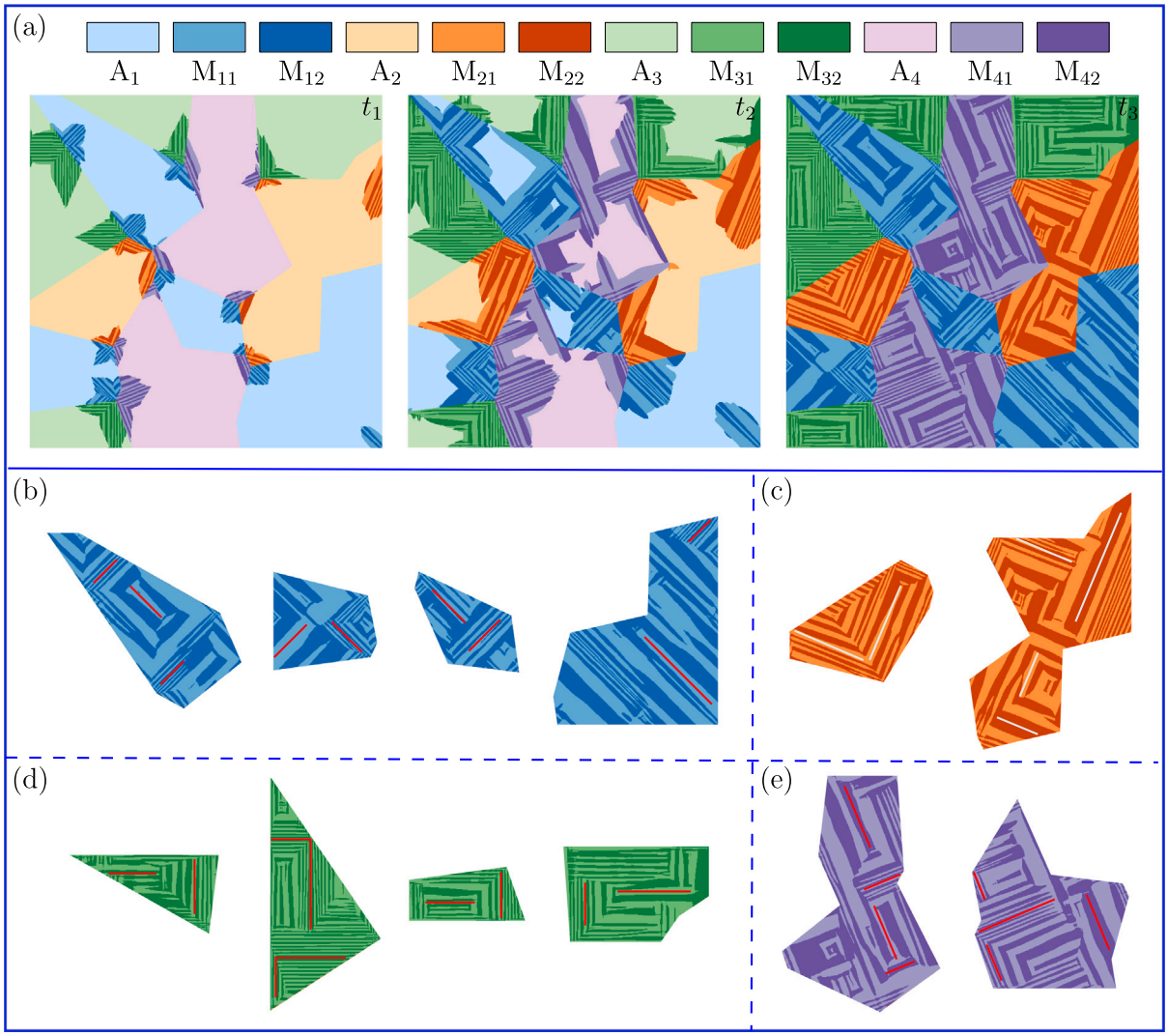

Fig. 6. MT in a polycrystalline domain under quasi-static conditions: (a) evolution of martensitic variants; (b–e) martensitic morphologies in austenite classes A_1–A_4, respectively.

Despite these simplifications, the simulations and analyses of wave-transformation interaction remain physically meaningful. Overall, the present work extends conventional quasi-static descriptions of MT by incorporating stress wave propagation as an intrinsic mechanical consequence of inelastic lattice reconfiguration in polycrystalline solids. The proposed framework highlights the fundamental role of transient stress fields in governing rapid microstructural evolution across grains and provides a foundation for future investigations of wave–transformation interactions in complex microstructures.

CRediT authorship contribution statement

Xiaoying Liu: Writing – review & editing, Writing – original draft, Visualization, Validation, Software, Methodology, Investigation, Formal analysis, Data curation, Conceptualization. **Daniel Schneider:** Writing – review & editing, Supervision, Software, Resources, Project administration, Methodology, Conceptualization. **Britta Nestler:** Writing – review & editing, Supervision, Software, Resources, Project administration, Funding acquisition, Conceptualization.

Declaration of competing interest

The authors declare the following financial interests/personal relationships which may be considered as potential competing interests: Britta Nestler reports equipment, drugs, or supplies was provided by state of Baden- Württemberg. If there are other authors, they declare that they have no known competing financial interests or personal relationships that could have appeared to influence the work reported in this paper.

Acknowledgments

We would like to thank the Helmholtz Association, Germany, for its support through the program "MSE No.: 43.31.01". The authors acknowledge support by the state of Baden-Württemberg through bwHPC.

Appendix

In the stress–velocity form of the governing equations for mechanical wave propagation, the coefficient matrices $\boldsymbol{C}^1$, $\boldsymbol{C}^2$ and $\boldsymbol{C}^3$ are constructed from the effective stiffness tensor $\boldsymbol{K}$ and the effective density $\bar{\rho}$ as follows:

$$\boldsymbol{C}^1 = \begin{pmatrix} 0 & 0 & 0 & 0 & 0 & 0 & K_{11} & 0 & 0 \\ 0 & 0 & 0 & 0 & 0 & 0 & K_{21} & 0 & 0 \\ 0 & 0 & 0 & 0 & 0 & 0 & K_{31} & 0 & 0 \\ 0 & 0 & 0 & 0 & 0 & 0 & 0 & 0 & 0 \\ 0 & 0 & 0 & 0 & 0 & 0 & 0 & 0 & K_{55} \\ 0 & 0 & 0 & 0 & 0 & 0 & 0 & K_{66} & 0 \\ \frac{1}{\bar{\rho}} & 0 & 0 & 0 & 0 & 0 & 0 & 0 & 0 \\ 0 & 0 & 0 & 0 & 0 & \frac{1}{\bar{\rho}} & 0 & 0 & 0 \\ 0 & 0 & 0 & 0 & \frac{1}{\bar{\rho}} & 0 & 0 & 0 & 0 \end{pmatrix}, \tag{A.1}$$

$$\boldsymbol{C}^2 = \begin{pmatrix} 0 & 0 & 0 & 0 & 0 & 0 & 0 & K_{12} & 0 \\ 0 & 0 & 0 & 0 & 0 & 0 & 0 & K_{22} & 0 \\ 0 & 0 & 0 & 0 & 0 & 0 & 0 & K_{32} & 0 \\ 0 & 0 & 0 & 0 & 0 & 0 & 0 & 0 & K_{44} \\ 0 & 0 & 0 & 0 & 0 & 0 & 0 & 0 & 0 \\ 0 & 0 & 0 & 0 & 0 & 0 & K_{66} & 0 & 0 \\ 0 & 0 & 0 & 0 & 0 & \frac{1}{\bar{\rho}} & 0 & 0 & 0 \\ 0 & \frac{1}{\bar{\rho}} & 0 & 0 & 0 & 0 & 0 & 0 & 0 \\ 0 & 0 & 0 & \frac{1}{\bar{\rho}} & 0 & 0 & 0 & 0 & 0 \end{pmatrix}, \tag{A.2}$$

$$\boldsymbol{C}^3 = \begin{pmatrix} 0 & 0 & 0 & 0 & 0 & 0 & 0 & 0 & K_{13} \\ 0 & 0 & 0 & 0 & 0 & 0 & 0 & 0 & K_{23} \\ 0 & 0 & 0 & 0 & 0 & 0 & 0 & 0 & K_{33} \\ 0 & 0 & 0 & 0 & 0 & 0 & 0 & K_{44} & 0 \\ 0 & 0 & 0 & 0 & 0 & 0 & K_{55} & 0 & 0 \\ 0 & 0 & 0 & 0 & 0 & 0 & 0 & 0 & 0 \\ 0 & 0 & 0 & 0 & \frac{1}{\bar{\rho}} & 0 & 0 & 0 & 0 \\ 0 & 0 & 0 & \frac{1}{\bar{\rho}} & 0 & 0 & 0 & 0 & 0 \\ 0 & 0 & \frac{1}{\bar{\rho}} & 0 & 0 & 0 & 0 & 0 & 0 \end{pmatrix}, \tag{A.3}$$

where $\bar{\rho} = \rho^{\alpha}$ in the bulk regions of phase α, whereas in diffuse interface regions, $\bar{\rho}$ is interpolated as $\bar{\rho} = \sum_{\alpha} \rho^{\alpha} h(\phi_{\alpha})$ (X. Liu et al., 2021).

Data availability

Data will be made available on request.

References

Achenbach, J. (2012). *Wave propagation in elastic solids*. Elsevier.

Ansari, T. Q., Huang, H., & Shi, S.-Q. (2021). Phase field modeling for the morphological and microstructural evolution of metallic materials under environmental attack. *Npj Computational Materials*, *7*(1), 143.

Arohi, A. C., Shekhar, S., & Sen, I. (2024). Stress-induced martensitic transformation during cold rolling of metastable β Ti–5Al–5V–5Mo–3Cr alloy. *Materials Science and Engineering: A*, *911*, Article 146910.

Asmaa, A. A., Lajos, D., László, Z. T., Irina, V. K., Yuriy, I. C., & Dezső, L. B. (2025). Acoustic emission during Lüders-band type martensitic transformation and thermal recovery in $Cr_{20}Mn_{20}Fe_{20}Co_{34.4}Ni_{5.6}$ high entropy shape memory single crystals. *Journal of Alloys and Compounds*, Article 180507.

Ball, J. A. D., Davis, C., Slater, C., Vashishtha, H., Said, M., Hébrard, L., Steinhilber, F., Wright, J. P., Connolley, T., Michalik, S., et al. (2024). Grain-level effects on in-situ deformation-induced phase transformations in a complex-phase steel using 3DXRD and EBSD. *Acta Materialia*, *265*, Article 119608.

Bauer, A., Vollmer, M., & Niendorf, T. (2021). Effect of crystallographic orientation and grain boundaries on martensitic transformation and superelastic response of oligocrystalline Fe–Mn–Al–Ni shape memory alloys. *Shape Memory and Superelasticity*, *7*(3), 373–382.

Behjati, P., & Najafizadeh, A. (2011). Role of chemical driving force in martensitic transformations of high-purity Fe-Cr-Ni alloys. *Metallurgical and Materials Transactions A*, *42*(12), 3752–3760.

Blaysat, B., Balandraud, X., Grédiac, M., Vives, E., Barrera, N., & Zanzotto, G. (2020). Concurrent tracking of strain and noise bursts at ferroelastic phase fronts. *Communications Materials*, *1*(1), 3.

Cahn, J. W., & Hilliard, J. E. (1958). Free energy of a nonuniform system. I. Interfacial free energy. *Journal of Chemical Physics*, *28*(2), 258–267.

Chapman, M., De Graef, M., James, R. D., & Chen, X. (2021). Quantitative analysis of compatible microstructure by electron backscatter diffraction. *Philosophical Transactions of the Royal Society, Series A*, *379*(2201), Article 20200112.

Chen, Y., Gou, B., Xu, X., Ding, X., Sun, J., & Salje, E. K. H. (2023). Multibranches of acoustic emission as identifier for deformation mechanisms in additively manufactured 316L stainless steel. *Additive Manufacturing*, *78*, Article 103819.

Chen, C. C., Lin, H. K., & Lan, C. W. (2014). Phase field modeling with large interface thickness and undercooling. *Journal of Crystal Growth*, *385*, 121–126.

Chen, J., Lu, S., Hou, Z., Song, W., Liu, Z., Wang, G., & Furuhara, T. (2024). Atomic-scale understanding of twin intersection rotation and ϵ-martensite transformation in a high Mn twinning-induced plasticity steel. *Acta Materialia*, *271*, Article 119832.

Chen, H. Z., & Shu, Y. C. (2013). Phase-field modeling of martensitic microstructure with inhomogeneous elasticity. *Journal of Applied Physics*, *113*(12).

Courant, R., Friedrichs, K., & Lewy, H. (1928). Über die partiellen differenzengleichungen der mathematischen physik. *Mathematische Annalen*, *100*(1), 32–74.

Daubner, S., Hoffrogge, P. W., Minar, M., & Nestler, B. (2023). Triple junction benchmark for multiphase-field and multi-order parameter models. *Computational Materials Science*, *219*, Article 111995.

Delcourte, S., & Glinsky, N. (2015). Analysis of a high-order space and time discontinuous Galerkin method for elastodynamic equations. Application to 3D wave propagation. *ESAIM. Mathematical Modelling and Numerical Analysis*, *49*(4), 1085–1126.

Dong, T., Liang, C., Su, Y., Zhao, T., Wang, D., Ren, X., & Wang, Y. (2023). Phase field simulations for the crossover from sharp martensitic transformation into smooth strain glass transition by fine precipitates. *Acta Materialia*, *245*, Article 118634.

Dumbser, M., & Käser, M. (2006). An arbitrary high-order discontinuous Galerkin method for elastic waves on unstructured meshes—II. The three-dimensional isotropic case. *Geophysical Journal International*, *167*(1), 319–336.

Feutang, F. K., Lejeunes, S., & Eyheramendy, D. (2025). A space-time approach for the simulation of brittle fracture with phase-field models in elastodynamics. *Computers and Structures*, *307*, Article 107616.

Ghasemi, A., & Vanini, S. A. S. (2023). Experimental and numerical investigation of martensite phase transformation in austenitic stainless steel subjected to ultrasonic nanocrystal surface modification at room and cryogenic temperatures. *Surface and Coatings Technology*, *474*, Article 130109.

Ginzburg, V. L., & Landau, L. D. (2009). On the theory of superconductivity. In *On superconductivity and superfluidity: A scientific autobiography* (pp. 113–137). Springer.

Gong, P., Kwok, T. W. J., Wang, Y., Dawson, H., Goodall, R., Dye, D., & Rainforth, W. M. (2025). A multi-scale microstructure to address the strength-ductility trade off in high strength steel for fusion reactors. *Nature Communications*, *16*(1), 2746.

Gong, N., Meng, T. L., Tan, C. K. I., Cao, J., Wei, Y., Maharjan, N., Tan, D. C. C., Xie, H., Lee, C. J. J., Misra, R. D. K., et al. (2023). High energy laser-shock induced phase transformation and micro-spallation on surface of stainless steels: The effect of stacking fault energy and deformation mechanisms. *Applied Surface Science*, *613*, Article 156013.

Guo, R., Zhang, P., Pan, J., Xu, J., Liu, L., Zhang, C., & Liu, L. (2024). Achieving prominent high-temperature mechanical properties in a dual-phase high-entropy alloy: A synergy of deformation-induced twinning and martensite transformation. *Acta Materialia*, *264*, Article 119591.

Hilding, D., & Schedin, E. (2002). Implementation of a material model for TRIP-steels in LS-DYNA and comparison with test results. In *4th European LSDYNA users conference, ulm*.

Hong, Y., Zhang, J., Wu, F., Zhang, Z., Luo, X., Li, X., Li, Z., Wang, Y., Chen, S., Yu, Y., et al. (2024). Coupling between phase transition and spallation in hierarchically structured high-strength martensitic steels under shock loading. *Engineering Fracture Mechanics*, *309*, Article 110431.

Jiang, J., Li, Y., Liu, Y., Kang, J., Li, X., Yuan, G., & Wang, G. (2025). Tailoring banded-equiaxed heterogeneous structure and martensite variants to achieve high toughness and high ductility in a newly designed 2.4 GPa high-strength steel. *Journal of Materials Science & Technology*, *231*, 270–285.

Jiao, Z., Li, Z., Wu, F., Wang, Q., Li, X., Xu, L., Hu, L., Liu, Y., Yu, Y., Hu, C., et al. (2023). Phase transition, twinning, and spall damage of NiTi shape memory alloys under shock loading. *Materials Science and Engineering: A*, *869*, Article 144775.

Kannenberg, T., Schöller, L., Prahs, A., Schneider, D., & Nestler, B. (2024). Microstructure evolution accounting for crystal plasticity in the context of the multiphase-field method. *Computational Mechanics*, *74*(1), 67–84.

Käser, M., & Dumbser, M. (2006). An arbitrary high-order discontinuous Galerkin method for elastic waves on unstructured meshes—I. The two-dimensional isotropic case with external source terms. *Geophysical Journal International*, *166*(2), 855–877.

Krauss, G. (2017). Tempering of lath martensite in low and medium carbon steels: assessment and challenges. *Steel Research International*, *88*(10), Article 1700038.

Lehnert, R., Franke, A., Biermann, H., & Weidner, A. (2021). Acoustic emission measurements on metastable austenitic steel oligocrystals. *Materials Science and Engineering: A*, *827*, Article 142066.

Lehnert, R., Remich, V., Gerstein, G., Motylenko, M., Müller, M., Krooß, P., Niendorf, T., Biermann, H., & Weidner, A. (2024). Unraveling factors affecting the reversibility of martensitic phase transformation in FeNiCoAlTi shape memory alloys: Insights from HR-EBSD and acoustic emission analysis. *Acta Materialia*, *276*, Article 120146.

Li, P., Wang, K., Chu, S., & Liu, G. (2024). Stress-induced martensite transformation and mechanical properties of fine-grained Ti-10V-2Fe-3Al alloy fabricated by friction stir processing. *Materials Science and Engineering: A*, *918*, Article 147416.

Li, B., Wang, L., Wang, B., Li, D., Oliveira, J. P., Cui, R., Yu, J., Luo, L., Chen, R., Su, Y., et al. (2022). Electron beam freeform fabrication of NiTi shape memory alloys: crystallography, martensitic transformation, and functional response. *Materials Science and Engineering: A*, *843*, Article 143135.

Li, B., Wang, B., Wang, L., Oliveira, J. P., Cui, R., Wang, Y., Zhu, G., Yu, J., & Su, Y. (2023). Effect of post-heat treatments on the microstructure, martensitic transformation and functional performance of EBF3-fabricated NiTi shape memory alloy. *Materials Science and Engineering: A*, *871*, Article 144897.

Li, Q., Zhou, L., Pan, Y., Ma, J., Zhou, X., Jiang, H., Xie, Z., & Fang, F. (2024). Formation of nano martensite grain with specific angle grain boundary during the drawing process of 316L stainless steel. *Materials Science and Engineering: A*, *897*, Article 146309.

Lian, Y., Hua, Y., Sun, J., Wang, Q., Chen, Z., Wang, F., Zhang, K., Lin, G., Yang, Z., Zhang, Q., et al. (2021). Martensitic transformation in temporally shaped femtosecond laser shock peening 304 steel. *Applied Surface Science*, *567*, Article 150855.

Liu, J., Binot, N., Delagnes, D., & Jahazi, M. (2021). Influence of the cooling rate below Ms on the martensitic transformation in a low alloy medium-carbon steel. *Journal of Materials Science & Technology*, *12*, 234–242.

Liu, C., Roters, F., & Raabe, D. (2023). Finite strain crystal plasticity-phase field modeling of twin, dislocation, and grain boundary interaction in hexagonal materials. *Acta Materialia*, *242*, Article 118444.

Liu, X., Schneider, D., Daubner, S., & Nestler, B. (2021). Simulating mechanical wave propagation within the framework of phase-field modelling. *Computer Methods in Applied Mechanics and Engineering*, *381*, Article 113842.
Liu, T.-W., & Wu, X.-L. (2024). Martensitic transformation pathways and crystallographic orientation relationships in steel. *Journal of Materials Science & Technology*, *174*, 74–84.
Lu, X., Lagnoni, M., Bertei, A., Das, S., Owen, R. E., Li, Q., O'Regan, K., Wade, A., Finegan, D. P., Kendrick, E., et al. (2023). Multiscale dynamics of charging and plating in graphite electrodes coupling operando microscopy and phase-field modelling. *Nature Communications*, *14*(1), 5127.
Moallemi, M., Kermanpur, A., Najafizadeh, A., Rezaee, A., Baghbadorani, H. S., & Nezhadfar, P. D. (2016). Deformation-induced martensitic transformation in a 201 austenitic steel: the synergy of stacking fault energy and chemical driving force. *Materials Science and Engineering: A*, *653*, 147–152.
Montes de Oca Zapiain, D., Stewart, J. A., & Dingreville, R. (2021). Accelerating phase-field-based microstructure evolution predictions via surrogate models trained by machine learning methods. *Npj Computational Materials*, *7*(1), 3.
Morito, S., Huang, X., Furuhara, T., Maki, T., & Hansen, N. (2006). The morphology and crystallography of lath martensite in alloy steels. *Acta Materialia*, *54*(19), 5323–5331.
Nagai, M., Higashitani, Y., Ashida, M., Kusakabe, K., Niioka, H., Hattori, A. N., Tanaka, H., Isoyama, G., & Ozaki, N. (2023). Terahertz-induced martensitic transformation in partially stabilized zirconia. *Communications Physics*, *6*(1), 88.
Nambu, S., Shibuta, N., Ojima, M., Inoue, J., Koseki, T., & Bhadeshia, H. K. D. H. (2013). In situ observations and crystallographic analysis of martensitic transformation in steel. *Acta Materialia*, *61*(13), 4831–4839.
Nataf, G. F., Romanini, M., Vives, E., Žužek, B., Planes, A., Tušek, J., & Moya, X. (2020). Suppression of acoustic emission during superelastic tensile cycling of polycrystalline $Ni_{50.4}Ti_{49.6}$. *Physical Review Materials*, *4*(9), Article 093604.
Niessen, F., Bhattacharyya, A., Gazder, A. A., Pereloma, E. V., & Lebensohn, R. A. (2022). Integrated multi-scale modeling of variant selection during stress-induced martensite formation in metastable β Ti-alloys. *Acta Materialia*, *240*, Article 118342.
Ohmer, D., Yi, M., Gutfleisch, O., & Xu, B.-X. (2022). Phase-field modelling of paramagnetic austenite–ferromagnetic martensite transformation coupled with mechanics and micromagnetics. *International Journal of Solids and Structures*, *238*, Article 111365.
Park, H. S., Kwon, O.-H., Baskin, J. S., Barwick, B., & Zewail, A. H. (2009). Direct observation of martensitic phase-transformation dynamics in iron by 4D single-pulse electron microscopy. *Nano Letters*, *9*(11), 3954–3962.
Qian, B., Li, X., Wang, Y., Hou, J., Liu, J., Zou, S., An, F., & Lu, W. (2024). An ultra-low modulus of ductile TiZrHfTa biomedical high-entropy alloys through deformation induced martensitic transformation/twinning/amorphization. *Advanced Materials*, *36*(24), Article 2310926.
Raabe, D., Sandlöbes, S., Millán, J., Ponge, D., Assadi, H., Herbig, M., & Choi, P.-P. (2013). Segregation engineering enables nanoscale martensite to austenite phase transformation at grain boundaries: a pathway to ductile martensite. *Acta Materialia*, *61*(16), 6132–6152.
Rezaee-Hajidehi, M., Sadowski, P., & Stupkiewicz, S. (2022). Deformation twinning as a displacive transformation: Finite-strain phase-field model of coupled twinning and crystal plasticity. *Journal of the Mechanics and Physics of Solids*, *163*, Article 104855.
Salama, H., Ali, M. A., Shchyglo, O., & Steinbach, I. (2024). Phase-field simulation framework for modeling martensite and bainite formation in steel. *Computational Materials Science*, *241*, Article 113033.
Salama, H., Shchyglo, O., & Steinbach, I. (2025). The interplay between the martensitic transformation rate and the rate of plastic relaxation during martensitic transformation in low-carbon steel, a phase-field study. *Npj Computational Materials*, *11*(1), 43.
Schneider, D., Schoof, E., Huang, Y., Selzer, M., & Nestler, B. (2016). Phase-field modeling of crack propagation in multiphase systems. *Computer Methods in Applied Mechanics and Engineering*, *312*, 186–195.
Schneider, D., Schoof, E., Tschukin, O., Reiter, A., Herrmann, C., Schwab, F., Selzer, M., & Nestler, B. (2018). Small strain multiphase-field model accounting for configurational forces and mechanical jump conditions. *Computational Mechanics*, *61*(3), 277–295.
Schneider, D., Tschukin, O., Choudhury, A., Selzer, M., Böhlke, T., & Nestler, B. (2015). Phase-field elasticity model based on mechanical jump conditions. *Computational Mechanics*, *55*(5), 887–901.
Schöller, L., Schneider, D., Herrmann, C., Prahs, A., & Nestler, B. (2022). Phase-field modeling of crack propagation in heterogeneous materials with multiple crack order parameters. *Computer Methods in Applied Mechanics and Engineering*, *395*, Article 114965.
Schoof, E. (2021). *Chemomechanische modellierung der wärmebehandlung von stählen mit der phasenfeldmethode*: *vol. 93*, KIT Scientific Publishing.
Schoof, E., Schneider, D., Streichhan, N., Mittnacht, T., Selzer, M., & Nestler, B. (2018). Multiphase-field modeling of martensitic phase transformation in a dual-phase microstructure. *International Journal of Solids and Structures*, *134*, 181–194.
Schwabe, S., Lünser, K., Schmidt, D., Nielsch, K., Gaal, P., & Fähler, S. (2022). What is the speed limit of martensitic transformations? *Science and Technology of Advanced Materials*, *23*(1), 633–641.
Sebdani, R. M., Bilan, H. K., Gale, J. D., Wanni, J., Madireddy, G., Sealy, M. P., & Achuthan, A. (2024). Ultrasonic Impact Treatment (UIT) combined with powder bed fusion (PBF) process for precipitation hardened martensitic steels. *Additive Manufacturing*, *84*, Article 104078.
Selzer, M. (2014). *Mechanische und strömungsmechanische topologieoptimierung mit der phasenfeldmethode* (PhD thesis), Karlsruher Institut für Technologie (KIT).
Shimokawa, T., Fujii, K., & Niiyama, T. (2024). Atomic simulation study of the factors affecting nucleation in deformation-induced martensitic transformation in grains and at grain boundaries in pure iron. *Acta Materialia*, *265*, Article 119629.
Shinohara, Y., Akabane, S., & Inamura, T. (2021). Analysis of variant-pairing tendencies in lenticular martensite microstructures based on rank-1 connection. *Scientific Reports*, *11*(1), 14957.
Shinohara, Y., Hishida, M., Tanaka, Y., & Inamura, T. (2023). Analysis of thin-plate martensite microstructure in steel focusing on incompatibility and its visualization. *Acta Materialia*, *259*, Article 119275.
Sreekala, S., & Ananthakrishna, G. (2003). Acoustic emission and shape memory effect in the martensitic transformation. *Physical Review Letters*, *90*(13), Article 135501.
Steinbach, I. (2009). Phase-field models in materials science. *Modelling and Simulation in Materials Science and Engineering*, *17*(7), Article 073001.
Su, Z., Yang, D., Yang, C., Fan, J., Yan, D., Peng, Y., & Wang, K. (2024). The influence of different ultrasonic impact treatment modes on microstructure and mechanical properties of 18Ni-300 steel fabricated by wire arc additive manufacturing. *Virtual and Physical Prototyping*, *19*(1), Article e2362424.
Sun, G., Lv, S., Zhang, Y., Xiao, L., Peng, Y., Zhu, Y., Wang, K., & Liu, J. (2026). Decoupling the orientation dependence of deformation-induced martensitic transformation via single-crystal micropillar compression. *Journal of Materials Science & Technology*, *244*, 80–87.
Tang, S., & Miao, J. (2024). Virtual clustering analysis for phase field model of quasi-static brittle fracture. *Computational Mechanics*, *74*(4), 875–888.
Tian, Z., Shang, C., Zhang, C., Zhou, X., Wu, H., Wang, S., Wu, G., Gao, J., Zhu, J., & Mao, X. (2025). Review of precipitation strengthening in ultrahigh-strength martensitic steel. *International Journal of Minerals, Metallurgy and Materials*, *32*(2), 256–269.
Tyc, O., Iaparova, E., Molnárová, O., Heller, L., & Šittner, P. (2024). Stress induced martensitic transformation in NiTi at elevated temperatures: Martensite variant microstructures, recoverable strains and plastic strains. *Acta Materialia*, *279*, Article 120287.
Wang, L., Dong, C.-f., Man, C., Hu, Y.-b., Yu, Q., & Li, X.-g. (2021). Effect of microstructure on corrosion behavior of high strength martensite steel—A literature review. *International Journal of Minerals, Metallurgy and Materials*, *28*(5), 754–773.
Wang, J., Huang, M., Hu, J., Wang, C., & Xu, W. (2021). EBSD investigation of the crystallographic features of deformation-induced martensite in stainless steel. *Journal of Materials Science & Technology*, *69*, 148–155.
Wang, X., Xie, Z., Li, X., & Shang, C. (2024). Recent progress in visualization and digitization of coherent transformation structures and application in high-strength steel. *International Journal of Minerals, Metallurgy and Materials*, *31*(6), 1298–1310.

Weidner, A., Vinogradov, A., Vollmer, M., Krooß, P., Kriegel, M. J., Klemm, V., Chumlyakov, Y., Niendorf, T., & Biermann, H. (2021). In situ characterization of the functional degradation of a [00$\bar{1}$] orientated Fe–Mn–Al–Ni single crystal under compression using acoustic emission measurements. *Acta Materialia*, *220*, Article 117333.

Weinberg, K., & Wieners, C. (2022). Dynamic phase-field fracture with a first-order discontinuous Galerkin method for elastic waves. *Computer Methods in Applied Mechanics and Engineering*, *389*, Article 114330.

Wilcox, L. C., Stadler, G., Burstedde, C., & Ghattas, O. (2010). A high-order discontinuous Galerkin method for wave propagation through coupled elastic-acoustic media. *Journal of Computational Physics*, *229*(24), 9373–9396.

Xiao, J. F., Jing, Y. D., Esmaeilzadeh, R., Cayron, C., & Logé, R. E. (2025). Microstructure and texture evolution in laser shock peened martensitic NiTi shape memory alloy. *Materials & Design*, *249*, Article 113555.

Xiong, J., Xu, B., & Kang, G. (2022). Phase field simulation on the martensite transformation and reorientation toughening behaviors of single crystal NiTi shape memory alloy: effects of crystalline orientation and temperature. *Engineering Fracture Mechanics*, *270*, Article 108585.

Yang, J., Wang, H., Li, Z., Zou, N., Yan, H., Yang, B., & Zuo, L. (2024). Crystallography of stress-induced martensitic transformation and giant elastocaloric effect in a $<001>_A$ textured $Ni_{27}Cu_{21}Mn_{46}Sn_6$ shape memory alloy. *Acta Materialia*, *263*, Article 119546.

Yao, S., Yu, J., Pei, X., Cui, Y., Zhang, H., Peng, H., Li, Y., & Wu, Q. (2024). A coupled phase-field and crystal plasticity model for understanding shock-induced phase transition of iron. *International Journal of Plasticity*, *173*, Article 103860.

Yin, W., Briffod, F., Hu, H., Yamazaki, K., Shiraiwa, T., & Enoki, M. (2024). Role of prior austenite grain boundary and retained austenite in strain localization of medium-carbon high-strength steels. *Acta Materialia*, *281*, Article 120422.

Zambrano, J., Toro, S., Sánchez, P. J., Duda, F. P., Méndez, C. G., & Huespe, A. E. (2024). An arc-length control technique for solving quasi-static fracture problems with phase field models and a staggered scheme. *Computational Mechanics*, *73*(4), 751–772.

Zhang, T., Bui, T. Q., Yu, T., Li, Y., & Natarajan, S. (2023). Quasi-static thermoelastic fracture: Adaptive phase-field modeling with variable-node elements. *Theoretical and Applied Fracture Mechanics*, *124*, Article 103811.

Zhang, N. B., Cai, Y., Fan, D., Zhao, X. J., Lu, L., Tang, Y., Li, Y. X., & Luo, S. N. (2024). Orientation relationships of impact-induced phase transformation in high entropy alloy $HfZrTiTa_{0.53}$. *Scripta Materialia*, *244*, Article 116007.

Zhang, L., Li, X., Ding, R., Zhang, C., Xu, B., Liu, J., Zhao, C., He, B., Liu, C., & Liu, Y. (2025). Role of martensite hardness in governing tensile behavior and local stress states in ferrite/martensite dual-phase steels. *Materials Science and Engineering: A*, Article 148841.

Zhang, X., Li, Z., Yang, B., Yan, H., Zhang, Y., Esling, C., Zhao, X., & Zuo, L. (2023). Reverse transformation crystallography of deformed martensite in Ni-Mn-Ga shape memory alloys. *Acta Materialia*, *243*, Article 118507.

Zhang, X., Shen, G., Li, C., & Gu, J. (2020). Phase-field simulation of austenite reversion in a Fe-9.6Ni-7.1Mn (at.%) martensitic steel governed by a coupled diffusional/displacive mechanism. *Materials & Design*, *188*, Article 108426.

Zhang, Z., Shen, F., Liu, H., Koenemann, M., & Münstermann, S. (2023). Temperature-dependent deformation and fracture properties of low-carbon martensitic steel in different stress states. *Journal of Materials Research and Technology*, *25*, 1931–1943.

Zhang, C., Zhang, Y., Esling, C., Zhao, X., & Zuo, L. (2017). Crystallographic features of the martensitic transformation and their impact on variant organization in the intermetallic compound $Ni_{50}Mn_{38}Sb_{12}$ studied by SEM/EBSD. *IUCrJ*, *4*(5), 700–709.

Zheng, S., Hou, X., Han, P., Xu, T., Shimada, T., & Wang, J. (2025). Tunable Lamb wave bandgap based on 90° diffuse domain walls in ferroelectric thin films. *Acta Materialia*, Article 121284.

Zhou, X., Li, Y., Han, Z., Liu, Z., Liu, K., Tu, Y., Fang, F., & Jiang, J. (2023). Unusual stress-induced martensite transformation in Ti-6Al-4V alloy enabled by solution treatment in the lower $\alpha+\beta$ regime. *Journal of Alloys and Compounds*, *956*, Article 170330.

Zhou, J., Xu, H., Shi, Y., & Li, J. (2021). Terahertz driven reversible topological phase transition of monolayer transition metal dichalcogenides. *Advanced Science*, *8*(12), Article 2003832.